



This is a repository copy of *Void nucleation and growth from heterophases and the exploitation of new toughening mechanisms in metals*.

White Rose Research Online URL for this paper:

<https://eprints.whiterose.ac.uk/200356/>

Version: Published Version

Article:

Guo, Y., Paramatmuni, C. and Avcu, E. orcid.org/0000-0002-3244-1316 (2023) Void nucleation and growth from heterophases and the exploitation of new toughening mechanisms in metals. *Crystals*, 13 (6). 860. ISSN 2073-4352

<https://doi.org/10.3390/cryst13060860>

Reuse

This article is distributed under the terms of the Creative Commons Attribution (CC BY) licence. This licence allows you to distribute, remix, tweak, and build upon the work, even commercially, as long as you credit the authors for the original work. More information and the full terms of the licence here:

<https://creativecommons.org/licenses/>

Takedown


If you consider content in White Rose Research Online to be in breach of UK law, please notify us by emailing eprints@whiterose.ac.uk including the URL of the record and the reason for the withdrawal request.



eprints@whiterose.ac.uk
<https://eprints.whiterose.ac.uk/>

Review

Void Nucleation and Growth from Heterophases and the Exploitation of New Toughening Mechanisms in Metals

Yi Guo ^{1,*}, Chaitanya Paramatmuni ^{2,*} and Egemen Avcu ^{3,4,*} 

¹ Shenyang National Laboratory for Materials Science, Institute of Metal Research, Chinese Academy of Sciences, Shenyang 110016, China

² Department of Materials Science and Engineering, University of Sheffield, Sheffield S1 3JD, UK

³ Department of Mechanical Engineering, Institute of Natural and Applied Sciences, Kocaeli University, Kocaeli 41001, Turkey

⁴ Ford Otosan Ihsaniye Automotive Vocational School, Kocaeli University, Kocaeli 41650, Turkey

* Correspondence: yguo@imr.ac.cn (Y.G.); c.paramatmuni@sheffield.ac.uk (C.P.); egemen.avcu@kocaeli.edu.tr (E.A.)

Abstract: Heterophases, such as precipitates, inclusions, second phases, or reinforcement particles, often drive void nucleation due to local incompatibilities in stresses/strains. This results in a significant life-limiting condition, as voids or their coalescence can lead to microcracks that reduce the ductility and fatigue life of engineering components. Continuum-mechanics-based analytical models have historically gained momentum due to their relative ease in predicting failure strain. The momentum of such treatment has far outpaced the development of theories at the atomic and micron scales, resulting in an insufficient understanding of the physical processes of void nucleation and growth. Evidence from the recent developments in void growth theories indicates that the evolution of voids is intrinsically linked to dislocation activity at the void–matrix interface. This physical growth mechanism opens up a new methodology for improving mechanical properties using hydrostatic pressurization. According to the limited literature, with a hydrostatic pressure close to 1 GPa, aluminium matrix composites can be made 70 times more ductile. This significant ductility enhancement arises from the formation of dislocation shells that encapsulate the heterophases and inhibit the void growth and coalescence. With further investigations into the underlying theories and developments of methods for industrial implementations, hydrostatic pressurization has the potential to evolve into an effective new method for improving the ductility and fatigue life of engineering components with further development.

Keywords: strength and ductility; void nucleation and growth; hydrostatic pressure; toughening



Citation: Guo, Y.; Paramatmuni, C.; Avcu, E. Void Nucleation and Growth from Heterophases and the Exploitation of New Toughening Mechanisms in Metals. *Crystals* **2023**, *13*, 860. <https://doi.org/10.3390/cryst13060860>

Academic Editors: Vasilis Karamitros, Umberto Prisco, Yang Liu and Mingyi Zheng

Received: 21 March 2023

Revised: 8 May 2023

Accepted: 10 May 2023

Published: 24 May 2023



Copyright: © 2023 by the authors. Licensee MDPI, Basel, Switzerland. This article is an open access article distributed under the terms and conditions of the Creative Commons Attribution (CC BY) license (<https://creativecommons.org/licenses/by/4.0/>).

1. Introduction

Ductile fracture is a common failure process within metallic structures [1]. The earliest studies to comprehend and predict the phenomenon of ductile fracture in metals and alloys subjected to complex stress state conditions date back more than a century [2]. The roles of void nucleation, growth, and coalescence in ductile fracture were identified in the 1940s, but the phenomenology of ductile fracturing was not well documented until the 1960s [3]. In their review paper on the failure of metals, Pineau et al. [4] noted that Tipper was the first to demonstrate that metals fail early due to void formation at second-phase particles almost 75 years ago [5]. Then, Goods and Brown reviewed the theories of void nucleation [6], including the void nucleation mechanisms derived from plastic deformation at grain boundaries, inclusions, and second-phase particles. Das and Chakravarty [7] have provided a comprehensive literature review of the different void nucleating sites for various alloys, indicating that micro voids intermittently form from a variety of elastic discontinuities such as inclusions, second phases, grain boundaries, etc. In an early review

by Curran et al. [8], experimentally observed nucleation sites of voids were listed along with their associated nucleation mechanisms and loading parameters.

Voids are the primary source of ductile fractures [9]. In structural metals deformed at room temperature, ductile fracture is typically initiated at sites where the compatibility of deformation is challenging [10]. It is often initiated by a decohesion or fracture of the heterophases (i.e., precipitates, inclusions, second phases, and reinforcement particles) [2] and grows through the plastic deformation of the surrounding matrix due to plastic strain influenced by hydrostatic stresses [11]. Then, the void coalesces by necking down the matrix material between its adjacent voids or via localized shearing between well-separated voids [3].

The phenomenology of ductile fracture is developed in the context of continuum damage mechanics, in which ductile fracturing occurs via damage accumulation through void nucleation, growth, and coalescence [3,12]. It is dependent on a number of factors, including the alloy composition, the content and distribution of the heterophases (precipitates, inclusions, second phases, and reinforcement particles), the grain size and micro-texture, the initial strain state, and the deformation temperature [12]. One of the most popular models accounting for ductile fracture is Gurson's void growth model [13], which links stress triaxiality and void volume fraction to plastic potential. Later, the model was improved by Tvergaard and Needleman [14] to better account for void nucleation and coalescence, and by many other researchers to account for the effects of visco-plasticity [15], plastic anisotropy [16], coalescence via internal necking [17], and failure under pure shear [18,19]. Obviously, these studies emphasised the significance of stress triaxiality on void growth through to fracture; however, they also leave an intriguing question unanswered about how exactly stress triaxiality interacts with the physical processes of void nucleation and growth. Xu et al. [20] analysed strain vs. void growth rate data from the literature and found that, under identical strain and stress triaxiality conditions, different alloys exhibited vastly different void growth rates, indicating that material-specific calibrations may be required for phenomenological models and that, in addition to stress triaxiality, the crystal plasticity of the matrix influences the evolution of the voids. On the other hand, recent molecular and dislocation dynamics simulations have provided valuable insights into the physical process of void growth under multiaxial loading conditions [21–24] and drawn forth several dislocation mechanisms [25] that may support mass transfer during void growth [26–29].

To sum up, understanding the physical processes of void nucleation and growth is important, yet a thorough review of the recent developments in physically based void growth mechanisms is lacking. This review serves the purpose of filling this gap. We also review a less recognized approach for mechanical property enhancement via hydrostatic pressurization, which not only highlights the importance of understanding the physical process of void growth but also opens up opportunities for designing materials that are resistant to the detrimental effects of heterophases on ductility.

The present review is based on scientific articles that have reported both numerical and experimental investigations on void formation in metals. The numerical studies based on continuum mechanical and physics-based formulations across length scales are reviewed in detail. In addition, the relevant laboratory and industrial experimental techniques for void detection and characterization are studied with emphasis on their merits, limitations, and scope for further developments. Reconciliations between hypotheses and experimental findings about void growth mechanisms are supported by figures. Using the Web of Science, SCOPUS, Science Direct, and Google Scholar databases, a comprehensive literature search was conducted. The literature search included the following keyword combinations: void nucleation, void growth, ductile fracture, dislocation/void growth, dislocation/void nucleation, hydrostatic stress/void growth, hydrostatic stress/void nucleation, molecular dynamic/void growth, molecular dynamic/void growth, stress triaxiality/void nucleation, stress triaxiality/void growth, void detection methods, XCT/void, SEM/void, in situ study/void, in situ study/ductile fracture, EBSD/void, acoustic emission, acoustic

emission/void detection, ultrasonic, ultrasonic/void detection, hydrostatic pressurization, diamond anvil cell, piston-cylinder instrument, dislocation at inclusion, dislocation at second-phase particle, hydrostatic pressure and strength, hydrostatic pressure and ductility, hydrostatic processing, and hydrostatic forming. The literature search revealed more than 300 articles, 193 of which were used to write the present review article. The literature was categorized in accordance with the sections outlined in the present review, and their abstracts, significant findings, and figures were reviewed in detail.

Section 2 includes background knowledge on void inspection methods, identifying those that are suitable for the online monitoring of void evolution. Although the phenomenological theories on void evolution have been thoroughly reviewed elsewhere, a brief introduction is given in Section 3, followed by a detailed discussion of some recent physics-based methodologies that account for local dislocation interactions. Section 5 demonstrates that, by exploiting the dislocation mechanisms of void nucleation and growth, hydrostatic pressurization significantly improves both strength and ductility. In Section 6, we conclude the article by putting forward our understanding and thoughts on how to further implement these toughening mechanisms to improve the strength and ductility of engineering components.

2. Methods to Evaluate Damage Evolution

The macroscopic stress–strain response of metals does not strongly fingerprint void nucleation events [10]. One elegant method previously proposed to detect the average overall void nucleation strain included pre-straining samples to various strains, followed by heat treatment to restore the strain-hardening capacity, and then loading again to failure. Assuming that the fracture strain is independent of pre-straining as long as there is no void nucleation, the level of pre-straining that leads to a reduction in the fracture strain after heat treatment indicates the void nucleation strain [30,31]. A slightly less laborious approach may involve the elastic modulus degradation technique [32,33], where multiple unloadings are performed during a tensile test, and the loss of elastic modulus is assumed to be related to the loss of load-carrying capacity due to the nucleation and subsequent evolution of the voids.

Caution must be taken while interpreting the results from such experiments, as the shape change of the sample gauge, especially during necking, may exaggerate the fraction of the damage extracted from the test results [34]. In such cases, finite element methods may be helpful in assisting the data interpretation [33,34]. While this approach is helpful in assessing either the overall void nucleation strain or the evolution of the void volume fraction during deformation, a local approach, through indentation testing [35,36], may be more appropriate for studying the influence of the local microstructure, such as the grain boundary character, and the shape, size, and spacing of the heterophases on the nucleation strain of the voids or cracks.

Based on the same principle of elastic stiffness degradation during damage evolution, an ultrasonic pulse-echo method has been utilized to evaluate the damage during deformation, as the ultrasonic wave velocity is proportional to the density and stiffness of materials. This technique has been applied to porous ceramics [37,38] and deformed metals [39,40]. Recently, the ultrasonic method has been applied in situ during fatigue testing to monitor the initiation of cracks [41], and its industrial relevance may be further enhanced by combining ultrasonic testing with machine learning [42]. While this technique is conceptually simple and relatively easy to implement in an industrial setting, a quantitative damage assessment must be accompanied by properly calibrated theoretical models so that the loss of wave speed and attenuation can be linked to the elasticity degradation [33]. Ultrasonic testing has gained popularity in porosity inspections of additive manufactured parts [43–46]. A comparison between ultrasonic detection and X-ray computed tomography (XCT) highlighted a relatively poor correlation of the porosity distribution between the maps of wave speed/attenuation and the XCT tomogram, except when the void size was

large. Furthermore, such measurements were subject to error due to the anisotropy of grains [43].

Numerous studies have found strong correlations between the build-up of dislocation structures and void nucleation [47,48], as discussed in detail in Section 4. The detection of dislocation activities and the associated critical events that lead to this void nucleation in bulk metallic materials is therefore of interest. Ultrasonic testing falls short in this regard due to its insensitivity to dislocation activity, while its close relative, acoustic emission, may be useful for studying dislocation accumulation, thereby predicting the onset of void nucleation at an early stage. Many different kinds of microstructure evolutions (e.g., dislocation co-operative motion, annihilation and breaking away from pinning points, deformation twinning, and particle breaking) release transient elastic waves that are readily detected in the form of acoustic emissions (AE) [49–52]. Typical AE signal analysis methods include the extraction of characteristics such as signal counts, pulse duration, AE power, amplitude, frequency, and information entropy [53–56], which are usually interpreted together with online or offline stress–strain data to deduce their correlations with microstructure evolutions. Furthermore, the technique is used to monitor the initiation and growth of fatigue cracks, as well as the decohesion and fracture of reinforcing particles within metal matrix composites [57,58]. While it is quite straightforward to correlate AE signals with the event of crack or void nucleation and to experimentally verify such correlations, correlating these AE signals with dislocation activity presents some challenges. As shown in Figure 1 [59], the AE signal peaks around the macroscopic yield point and decays quickly during work hardening, which has been observed in virtually all experimental investigations on pure single and polycrystalline metals with various types of crystal structures during monotonic plastic deformation [60–62].

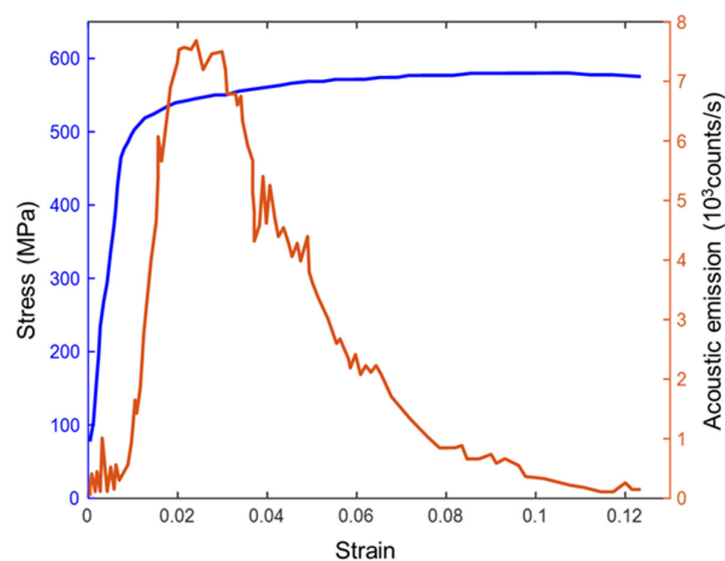


Figure 1. Tensile stress–strain curve and the corresponding acoustic emission signal for a 7075-T6 specimen. Figure reproduced from [59]. Copyright 2023, Elsevier.

Earlier studies have attributed the AE pulse rate to the rate of total dislocation multiplication [63], the number of mobile dislocations [59], and the rate of mobile dislocation multiplication [64]. Based on an argument involving dislocation velocity during plastic deformation, James and Carpenter [64] ruled out the possibilities from the first two mechanisms and argued that the AE pulse rate is proportional to the rate of change in the mobile dislocation densities:

$$pulse\ rate \cong 10^{-4} \left(\frac{dN_m}{dt} \right) \quad (1)$$

The fundamental mechanism underlying Equation (1) was postulated to be the dislocation breaking away from the pinning points in a collective manner that involves a

total dislocation length of several thousand centimetres [64]. In fact, determining the AE sources and using the AE to identify the deformation mechanisms seem to be long-standing problems. Numerous models have been proposed based on the dislocation mechanism alone. Apart from what has been introduced above, others include the formation of a slip line [65], dislocation multiplication from the Frank–Read source [66], an acceleration or deceleration of the dislocation movement [67], and an annihilation of the dislocations, including escape to a free surface [68–70]. Based on a literature review, Vinogradov and Merson [71] presented a detailed argument on the contribution of each dislocation mechanism to the observed AE signals and concluded that dislocation escape to the free surface is the most probable mechanism responsible for the peak AE. This hypothesis was supported by a compression test on solid and hollow cylindrical copper samples [72], which indicated that the AE power increased with an increasing hollow volume, even though the volume of the material decreased. Based on this argument, an expression was put forward linking the AE power to the surface area of the samples [71]:

$$P_{AE} = D \frac{\mathcal{V}_0^2 S \dot{\epsilon}}{\sigma^2} \quad (2)$$

where \mathcal{V}_0 is the dislocation velocity in the bulk, S is the surface area of the sample, $\dot{\epsilon}$ is the strain rate, σ is the flow stress, and D is a constant for a given material. In addition, another model is also proposed, linking AE power to the mechanical properties of the materials [73]:

$$P_{AE} = K_{AE} \rho_m \frac{\dot{\sigma}}{\sigma} \quad (3)$$

where K_{AE} is a constant and fraction of the total plastic power released in the AE form and ρ_m is the mobile dislocation density. This model assumes that the density of the mobile dislocation quickly decreases after the initial yielding, so that the experimentally observed AE count rate, with an initial sharp peak followed by a sharp decrease, can be reproduced. The authors argued that this assumption is valid based on a thermal activation analysis of the dislocation glide of the Arrhenius-type formulation for the plastic strain rate [74,75].

As Vinogradov and Merson [71] correctly pointed out, a practical application that may steer the future development of AE techniques is the diagnosis of microstructure evolutions from AE signals. This is a non-trivial task, since the recorded AE signal is an overlap of individual AE sources with distinct waveforms and power spectral density functions (SDF). In the context of this review, it would be of interest to comprehend the relationship between the dislocation density and the nucleation of voids via AE so that online monitoring can detect early signs of damage. Although this has been indirectly achieved through AE signal analyses and mechanical damage simulations using a Gurson-type model [76], more sophisticated micro-mechanical testing [77,78] together with AE monitoring to resolve the temporal correlations between the AE signals and void evolution, deserve further efforts. Furthermore, advanced signal processing techniques [79,80] may help in resolving AE waveforms and SDFs and are applied in the online monitoring of void volume fraction during additive manufacturing [81]. It is foreseeable that, with further development, AE will become a potent non-destructive online monitoring technique for the early detection of damage nucleation.

The above mentioned ultrasonic and AE methods are probably most suitable for engineering inspections and online monitoring. However, when the 3D characteristics of inclusions, precipitates, or voids are of interest, X-ray computed tomography (XCT) may be useful for understanding the influences of microstructural features on void nucleation and growth mechanisms. XCT can be applied to samples or components with length scales ranging from meters to nanometres [82]. X-ray tomograms are formed by stacking slices of images reconstructed from a series of projections (or radiographs) through the most commonly used filtered back-projection algorithm [83]. The contrast on each projection may derive from either attenuation contrast (or absorption contrast) or phase contrast, depending on how the X-ray interacts with matter. For the former, the contrast

is determined by the line integral of the attenuation of the beam as it passes through the object. Each reconstructed slice represents a map of the linear attenuation coefficient for the corresponding segment in the object [84]. The attenuation contrast method is suitable for distinguishing objects with distinct atomic numbers, such as distinguishing inclusions/voids and the hosting materials. Particularly, XCT has enabled the analysis of void growth over time on a single sample during mechanical testing [85]. For instance, Jia et al. [86] have examined the micro ductile fracture mechanisms of a high-Mn steel via in situ three-dimensional X-ray CT, enabling them to study void growth in ductile fracture. Figure 2 demonstrates a 3D rendering of the void growth in high-Mn steel samples with increasing tensile strain. In addition to this, the volume growths of the presented voids are also quantitatively presented in Figure 2. The volume of the voids is significantly increased (more than 30 times for some of the voids) with an increasing strain, revealing that voids grow along the principal tensile direction and change in shape (Figure 2) [86]. In another recent study, the influence of hydrogen presence on the void growth (i.e., ductile failure) of pipeline steel has been qualitatively and quantitatively examined via high-resolution X-ray CT scans of interrupted tests at different strains (Figure 3a) [87]. It has been shown that hydrogen charging accelerates void growth, as revealed by comparing the void volumes of uncharged (top) and hydrogen-charged (bottom) specimens (Figure 3b).

Often, information regarding the grain or phase boundaries is required in order to correlate the location of the voids within microstructures. In many cases, the materials across the grain or phase boundaries may not have sufficient density differences to generate a noticeable attenuation contrast; therefore, one needs to resort to either phase contrast [88] or diffraction contrast [89], the details of which can be found elsewhere [90–92]. Synchrotron X-ray sources provide much higher photon flux than laboratory tube sources, allowing for a complete scan within seconds [82], therefore enabling in situ 4D studies [93,94] with extreme temporal resolutions.

In situ mechanical testing performed inside scanning electron microscopy (SEM) has gained traction in recent years, due to its high spatial resolution and flexibility in integrating with various quantitative analysis tools such as high angular resolution EBSD (HR-EBSD) [95], digital imaging correlation (DIC) [96], and electron channelling contrast imaging (ECCI) [97]. These provide a unique opportunity to study the mechanisms of void nucleation and growth in the context of the crystallography and plasticity of the surrounding matrix. Unfortunately, the application of quantitative in situ testing to void nucleation and growth is scarce in the literature, as it seems that most efforts have been devoted to numerical simulations for understanding this phenomenon.

Figure 4 demonstrates a few distinct dislocation activities that form around the voids. Note that the voids in the copper (Figure 4a) developed a relatively homogeneous pattern of slip traces in comparison to those in the Ni superalloy (Figure 4b), resulting in a significantly faster void growth rate [25]. In contrast, no obvious slip traces were found around the voids in the titanium (Figure 2c), but rather very fragmented grain structures, which may form due to dislocation entanglement near the void surface. The surface traces demonstrated in Figure 4d stem from a so-called dislocation channelling deformation, which is commonly observed in deformed irradiated metals and is perhaps the simplest way to visualize how dislocations may contribute to void growth. This is evidenced by the two near vertical slip traces located at the top of the void, which tend to “pull-up” the upper part of the void into an elongated shape. This phenomenon implicitly correlates with a void growth mechanism by the gliding of a pair of anti-parallel dislocations [25]. The evolution of meso-scale dislocation structures was studied in situ under an SEM combined with elastic strain measurements using HR-EBSD [25]. Here, the resolved shear stresses on the 12 slip systems were analysed to identify the potential location around the void where dislocation could potentially be emitted. It was demonstrated that image stress tends to pull dislocations towards the void surface. This phenomenon reduces the tendency for dislocation emission from the void surface and therefore decreases the void growth rate.

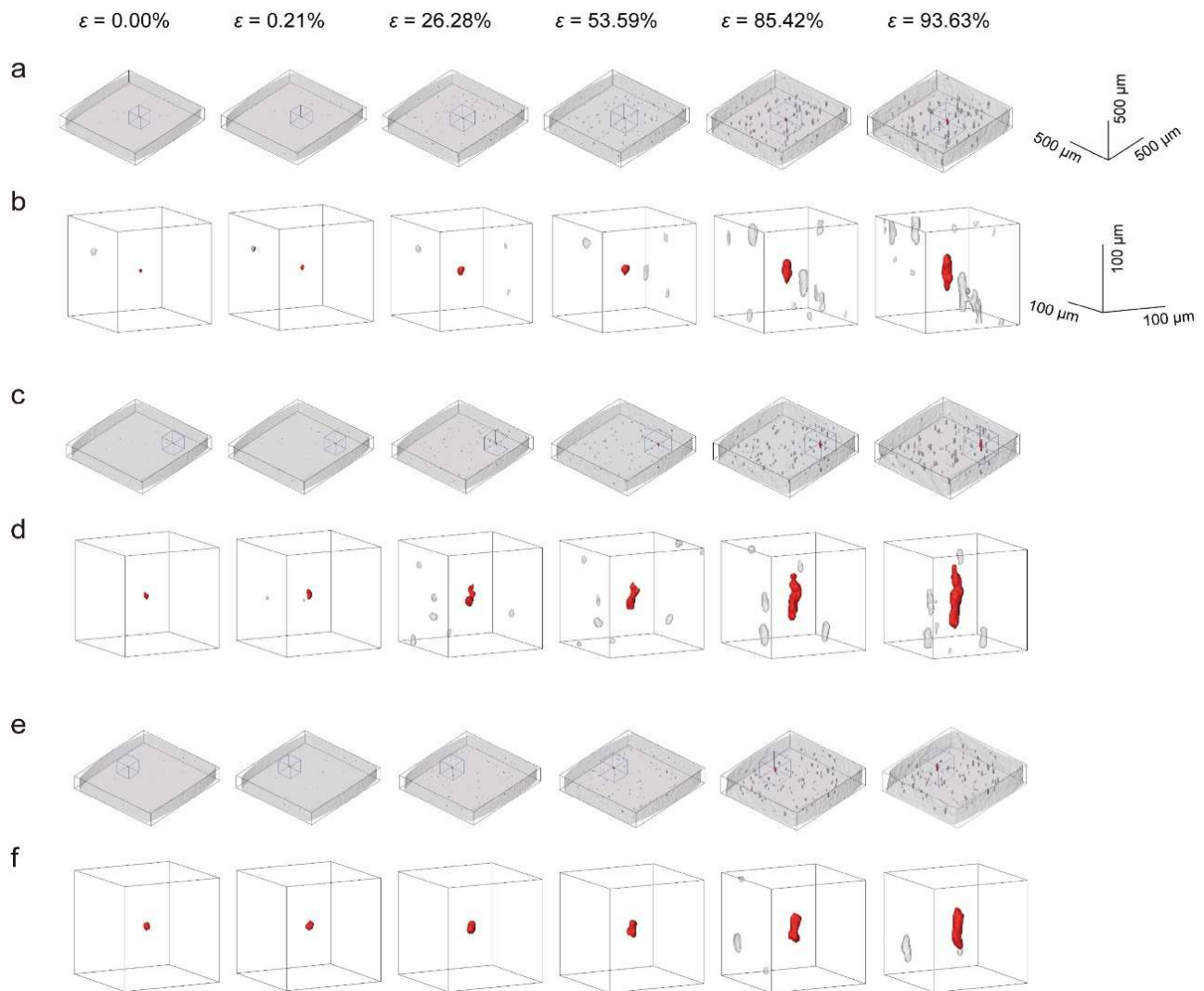


Figure 2. Void growth in a high-Mn steel sample rendered in three dimensions. The images in panels (b,d,f) are magnified versions of the grey cubic regions shown in panels (a,c,e). 3D volume size in panels (b,d,f) is $150 \times 150 \times 150 \mu\text{m}^3$. Reproduced under the terms of the CC-BY Creative Commons Attribution 4.0 International License [86]. Copyright 2023, The Authors, published by Elsevier.

A quantitative understanding of the local plasticity around voids as it evolves with external loading is important for assisting the design of microstructures that are more ductile and damage tolerant and, perhaps more fundamentally, for finding the missing link between phenomenological parameters, such as stress triaxiality, and the physical process of void growth. As will be discussed in the following sections, a step forward from phenomenological simulations of damage evolution is needed to bridge the macroscopically measurable quantities to the microstructural factors governing void evolution, from which the influence of voids on mechanical properties may be better predicted and the performance of materials may be better designed.

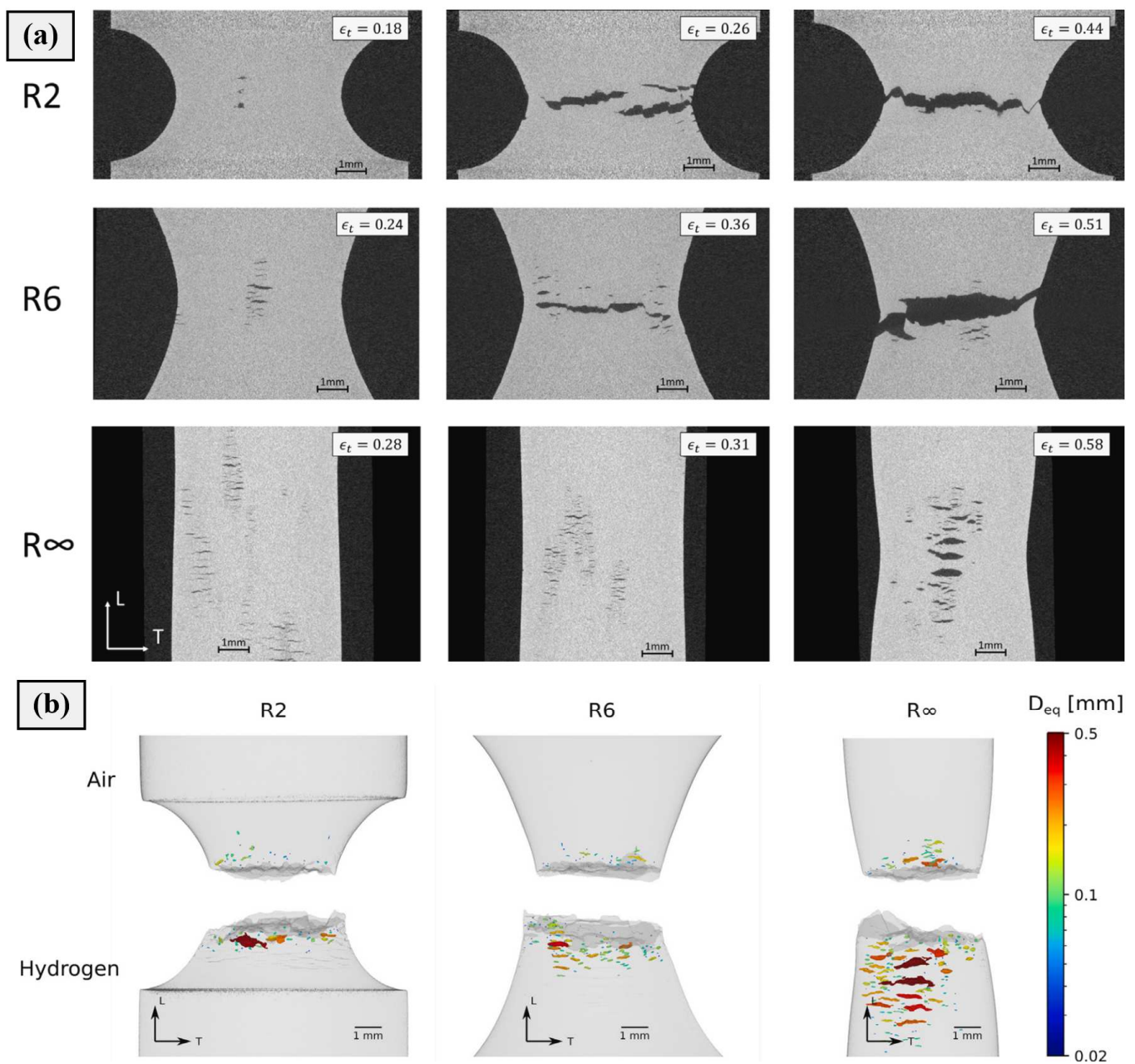


Figure 3. (a) 2D slices of the reconstructed X-ray volumes of hydrogen-charged tensile tests from interrupted tensile tests; and (b) thresholded volumes of uncharged (**top**) and hydrogen-charged (**bottom**) samples. Damage is visualized based on the equivalent diameter. R ∞ denotes smooth tensile specimen, whereas R2 and R6 refer to double-notched specimens featuring 2 mm or 6 mm radius notches, respectively. Reproduced with permission [87]. Copyright 2023, Elsevier.

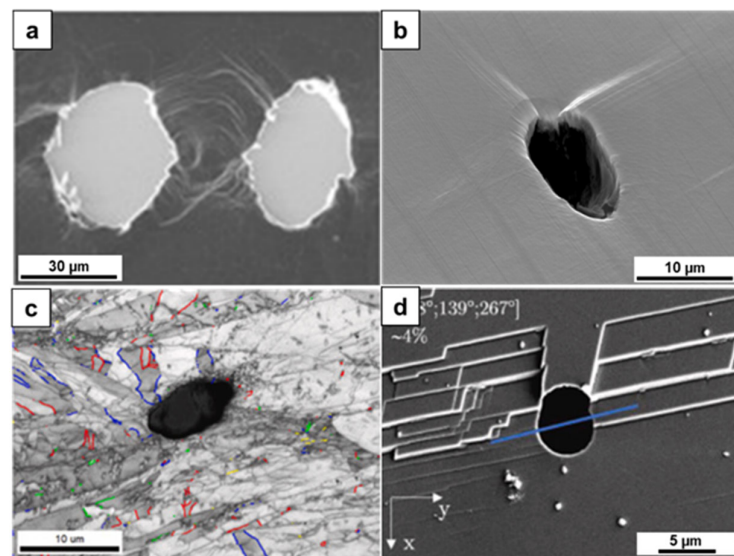


Figure 4. Dislocation activity around voids in copper [98] (a), single crystal Ni superalloy [25] (b), titanium [99] (c), and high energy proton irradiated 304 austenitic stainless steel [100] (d). (a) Reproduced with permission [98]. Copyright 2016, Elsevier. (b) Reproduced with permission [25]. Copyright 2021, Elsevier. (c) Reproduced with permission [99]. Copyright 2023, Elsevier. (d) Reproduced with permission [100]. Copyright 2019, Elsevier.

3. Theories on Damage Evolution—Continuum Approach

Numerous models and criteria for void nucleation have been developed over the past few decades, based on both dislocation and continuum mechanics theories [10,101]. For void nucleation at precipitate interfaces, it is suggested and widely accepted that particle size determines the scope of the application of an individual model [101]. When particles are submicron in size, dislocation-based models are necessary [10], while continuum-mechanics-based models are used when these particles are larger than 1 μm . However, evidence shows that 1 μm may not be a strict delineation [6]. After all, the argument on such a scale limit is a rationalization of whether a simplified approach can be used, while the choice of a suitable framework depends on the expected level of complexity in the models, which is driven by the intended outcome of the numerical analyses.

As Wcislik et al. [101] have recently discussed, the void nucleation and growth in ductile materials are strongly dependent on stress triaxiality (i.e., the ratio of von Mises equivalent stress to mean stress (hydrostatic pressure)). A high stress triaxiality means that hydrostatic stress is significant, for instance in the vicinity of geometric notches, whereas a low stress triaxiality corresponds to stress states where deviatoric stress dominates, for example, uniaxial tension conditions. The influence of stress triaxiality on the strain required for void nucleation has been extensively studied in the existing literature [11]. It has been reported that stress triaxiality governs whether particle cracking or particle-matrix decohesion occurs first [102]. For instance, Pathak et al. [102] recently proposed a stress-state dependent nucleation model by introducing a nucleation strain surface as a function of stress triaxiality via the modification of a previous nucleation model. Bonora et al. [103] proposed a new continuum-mechanics-based model that provides a relationship between the damage threshold strain dependence and the stress triaxiality, thereby enabling the analysis of the nucleation strain as a function of the stress triaxiality. In addition to stress triaxiality, the literature mentions the influence of the Lode parameter on the void nucleation, where the Lode parameter refers to the third tensor invariant [11]. As briefly reviewed by Wcislik et al. [11], the value of the Lode parameter has little effect on the void nucleation strain. However, it plays a significant role, as interfacial cracks nucleate from different positions for various Lode parameters and propagate in various patterns. This is caused by the Lode parameter modifying the principal stress distribution, even at constant

triaxiality values. Although the influence of the Lode parameter has been extensively studied in void growth models, only a small number of studies have considered the Lode parameter as a significant factor in predicting void nucleation [3,102].

In general, there are three fundamental groups of void nucleation criteria: stress, strain, and energy [101]. Depending on the analysed void nucleation mechanism (particle fracturing or decohesion from the matrix), the stress criterion necessitates the local attainment of the critical value in the particle itself or at the interface. As Pineau et al. [10] described in detail, void nucleation is caused by particle fracturing when the energy release rate exceeds the particle fracture toughness, which can be interpreted as an effective critical stress condition within the particle; thus, linear-elastic fracture mechanics arguments can be used to justify a simple one-parameter condition. This type of model can also be formulated in terms of stress, such that particle fracture occurs when the maximum principal stress inside the particle exceeds the material strength [101]. In contrast, the linear fracture mechanics approach is irrelevant in the case of an interface fracture if the matrix surrounding the particle is deforming plastically [10]. Due to the significant plastic deformation that occurs in the matrix surrounding the particle, the mechanism of void nucleation via particle–matrix decohesion typically does not permit the definition of a simple criterion based on a single parameter [101]. In such cases, the energy condition is easily satisfied, but sufficient plastic deformation must be accumulated at the interface to raise the stress above the critical strength [10]; thus, it is hypothesized that both the critical stress at the interface and the energy criterion must be satisfied simultaneously [101].

Although it is suggested that high local tensile normal stresses are necessary for void nucleation, pre-existing voids within the microstructure prior to mechanical loading, possibly coming from manufacturing processes, can bypass the requirement for the attainment of a critical stress condition for nucleation [104]. Thus, it is very challenging to unequivocally generalize how one can model this void nucleation by considering numerous criteria, loading states, and microstructural features. Despite the efforts outlined in this section, so far, it has not yet been possible to define one universal condition that can be applied regardless of the microstructural feature, stress state, and other factors, and determining whether void nucleation is controlled by stress or strain is especially difficult [101]. In addition, apart from the large second-large particles that cause void nucleation, large non-metallic inclusions, such as oxides and sulfides, are frequently cracked or deboned prior to the plastic deformation, making void nucleation relatively easy [9]. Furthermore, to create a more accurate model for predicting void nucleation, the critical stress and particle fracture toughness must be determined experimentally, which is not an easy task.

The earliest phenomenological models describing the growth of isolated voids in ductile metals were developed by McClintock [105] and Rice and Tracey [106] almost 55 years ago. Following these models, the micromechanics-based Gurson model [13] and the modified Gurson models considering the void interactions during ductile failure were proposed (e.g., extended by Tvergaard [107,108], Chu and Needleman [109], and Tvergaard and Needleman [14]). The Gurson and its modified models consider the void coalescence, as opposed to the Rice and Tracey model, which is based on a single void, and these models examine the plastic flow in a porous medium based on the assumption that the material behaves as a continuum [9]. The empirical Gurson–Tvergaard–Needleman (GTN) model incorporates the micro-scale effects of void nucleation, growth, and coalescence into the macro-scale constitutive law. As a result, it ties the behaviour of the macrofracture to the micro-scale evolution of damage and is therefore widely employed in numerical simulations [110,111]. The GTN model implies that the material is homogeneous and behaves as a continuum. The voids are accounted for by influencing the global flow behaviour of the material and their effects on this behaviour are averaged [85]. The yield surface in the GTN model is dependent on the hydrostatic stress, whereas classical plasticity implies that this yielding is independent of hydrostatic stress [9]. For this modification to classical plasticity, the term “strain softening” is introduced. The strain softening term accounts for the initiation, growth, and coalescence of the voids and is used in conjunction

with Von Mises yield criterion-driven matrix material hardening [85]. It is hypothesized that ductile failure results from a plastic instability that causes a band of localized deformation, which occurs due to the strain softening induced by hydrostatic stress [9]. Although the GTN model has been widely used to analyse the ductile failure of various metals, the model in its basic form yields inaccurate results under relatively high-stress conditions [111] or shear dominant loadings [101]. Moreover, the model cannot estimate the necking instability between voids, since it does not account for discrete voids [9]. In light of these limitations, as summarized by Lee et al. [111], researchers have implemented additional modifications, such as combining the model with the Johnson–Cook model to better describe the ductile failure under high strain rate states, enhancing the model for low stress triaxiality conditions and incorporating damage mechanisms due to shear.

The Gologanu–Leblond–Devaux (GLD) model was developed by expanding the Gurson model to include void shape effects [112]. Aldakheel et al. [113] proposed a modified Gurson-type plasticity model at finite strains by combining the GTN-type plasticity model with a new evolution equation for the crack phase field. The proposed model is capable of modelling the fundamental phenomena of ductile failure, such as the experimentally observed cup–cone failure surfaces, using an approach with low computing costs [114]. Besides the outlined GTN-based models, other phenomenological models (e.g., the Johnson–Cook model [111,114]) have also been used to evaluate the ductile failure of metals, which have been extensively reviewed in the literature [3,4,10,112].

Even though numerous modifications have recently been made to the void growth models to consider various parameters during the ductile fracturing (e.g., strain hardening, strain rate dependency, and void size, etc.), these void growth models use several simplifications related to the material properties (more particularly, the microstructural features). Although the simplified approaches are useful for predicting the forming limit or failure condition, they are ineffective at informing on how to improve these properties through microstructure engineering. Clearly, future research is necessary for developing void nucleation and growth models specifically focused on dislocation-based mechanics that can address the physical processes of the void nucleation and growth within particular microstructures.

4. Theories on Damage Evolution—Physics-Based Mechanisms

Thus far, the classical models that attempt to understand the evolution of voids by assuming the material as an isotropic and homogeneous medium have been discussed. These models are being significantly extended to account for anisotropy, the heterogeneity in the material’s microstructure, and its deformation response. This section provides an overview of the physics-based mechanisms of void nucleation and growth that are influenced by local plasticity and material heterogeneity.

4.1. Void Nucleation and Growth Mechanisms at Nano- and Sub-Micron Scale: Atomistic Simulations and Dislocation Dynamics

The nucleation of voids is a complex phenomenon that makes simulating this process difficult. The ambiguity arises in defining the precise stage at which a void can be flagged to have nucleated within the microstructure. While it may be reasonable to define the accumulation of critical stress as the nucleation criterion, it is also acceptable to define either lattice delamination or dislocation-assisted delamination as the initial stage of this nucleation. Therefore, it remains a debatable topic that has gained traction in recent years.

The homogeneous nucleation of voids occurs in three stages—the accumulation of local critical stresses, lattice instability, and nucleation. Pang et al. [115] studied the nucleation of the dislocations and voids in single crystal FCC metals, suggesting that exceeding a critical strain during plastic deformation causes the formation of stacking faults that grow to intersect and generate pillar-like vacancy strings located at their intersections, as shown in Figure 5. These vacancy strings then grow into voids by emitting dislocations when the stress around them exceeds the critical values. While several such vacancy strings

form within the microstructure, only some strings grow into voids, which relax the local stresses and suppress the formation of other voids at the vicinity (observe that only the vacancy string in Figure 5 grows to become a void). Agarwal and Dongare [116] studied the evolution of defects in single crystal Al and reported the nucleation of voids in a dislocation-free microstructure loaded along the $\langle 110 \rangle$ direction, due to the limited mobility of plastic waves during shock compression. In addition, this study demonstrated that the presence of stair-rod partials in the microstructure significantly improves the capability of metals to nucleate voids under triaxial stresses.

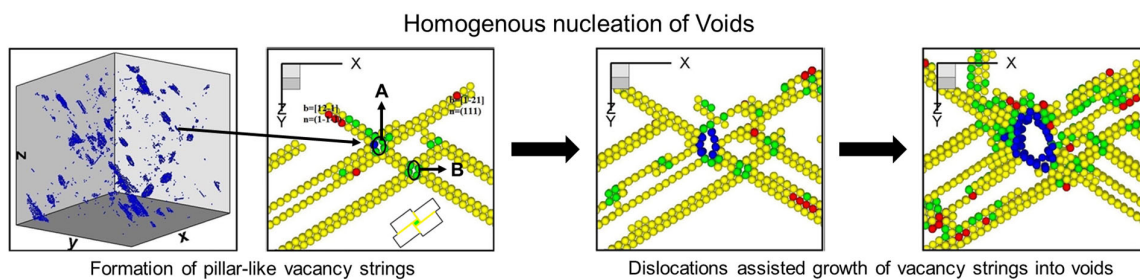


Figure 5. The void nucleation process illustrating homogenous nucleation [116]. In homogenous nucleation, stacking faults intersect to form pillar-like vacancy strings, which grow into voids by emitting dislocations when the local stresses exceed critical values. Reproduced under the terms of the CC-BY Creative Commons Attribution 4.0 International License [116].

In contrast, it is generally accepted that the heterogeneous nucleation process at the precipitate–matrix interface comprises the accumulation of critical stress, the dislocation-free delamination at the interface, and the dislocation-assisted growth of the delaminated region. Cui and Chen [117] studied the nucleation of voids at the interface of Cu matrix and Si particles. The nucleation in their study occurred at the dislocation-free Cu–Si interface along the loading direction after the local stress exceeded a critical value. Then, the subsequent delamination from the precipitate was supported by the formation of local dislocation structures. These dislocations at the interface later formed secondary frustum-like asymmetric structures that facilitated local material transport, leading to further debonding and complete void nucleation. Pogorelko and Mayer [118] made similar observations in their void nucleation studies, with Cu particles embedded in an Al matrix. Pogorelko and Mayer [119] extended this study by incorporating Ti and Mg precipitates within the Al matrix to investigate the effect of precipitate strengths on the nucleation of voids. They observed that the void nucleation followed the stress concentration, dislocation-free delamination, and dislocation-assisted growth processes in the case of an Al–Ti system, wherein the void nucleated at the interface within the Al matrix. In contrast, the void nucleated within the Mg precipitate in the Al–Mg system and propagated into the Al matrix. Recently, Zhao et al. [120] suggested that the initial delamination took place with an increase in the displacement of atoms, without the formation of local dislocation structures. This stage, termed as the lattice-trapped delamination process, was followed by the dislocation-assisted growth of the nucleated void. Furthermore, Paul et al. [121] studied the effect of loading directions on the failure of nano-crystalline Al and reported the nucleation of voids at the triple junction in all the loading directions.

After nucleation, voids grow through local material transport, which is supported by the evolution of dislocation structures at their vicinity. In their theoretical analyses, Lubarda et al. [26] proposed the growth of existing voids through the continuous emission of dislocations, which interact to generate prismatic and/or shear loops, enabling mass transport and leading to void growth. In addition, Lubarda et al. [26] also suggested that the critical stress required for dislocation emission decreases with increasing void size. While the formation of prismatic loops was proposed in their study as one of the growth mechanisms [26], only shear loops are observed in the majority of numerical studies (e.g., [122–125]). The formation of prismatic loops driven by the size of the void was also

observed in the atomistic simulations of Xu et al. [126]. Zhao and Liu [127] identified four distinct stages in void growth: a constant stage during elasticity, a slow growth stage characterized by the accumulation of dislocations, a rapid growth stage associated with the rapid formation of dislocations that speeds up the local material transport, and finally a linear growth stage caused by the stress relaxation and severe plasticity at the vicinity of the void. These stages, if not explicitly mentioned, have also been observed in other studies (e.g., [117]).

The mechanism of the formation of shear loops depends on the location of the void, the crystal structure of the matrix, and the temperature. The initiation of shear loops on the void surface occurs at the onset of plasticity, consisting of a stacking fault ribbon bound by two Shockley partial dislocations. With further deformation, more shear loops approximately bowed into semi-circles form on the various {111} planes, which interact with the existing shear loops to produce Lomer–Cottrell sessile dislocations that lead to work hardening at the vicinity of the void. The further increase in the applied load leads to the generation and propagation of more shear loops, resulting in complex dislocation structures [124,128]. Similarly, Traiviratana et al. [122] also showed that a similar growth mechanism is energetically feasible for shear loops bound by perfect dislocations. In the case of BCC metals deformed at 10 K, Xu et al. [126] showed that the $\langle 111 \rangle$ {110} perfect dislocations originate from the void source, propagate, and interact to form stable, non-coplanar, two-fold screw cores, leading to the formation of Frank–Read dislocation sources. The perfect dislocations continue slipping to form shear loops. Tang et al. [129] performed a similar investigation at 300 K and observed the formation of {112} shear loops by adjacent {110} stacking faults intersecting at the void surface at 45° . Furthermore, Zhang et al. [130] studied the growth of a void located at a twin boundary in nano-twinned Ni. The void growth resulted from the material transport, which was driven by the emission of leading partial dislocations that interacted to form sessile stair-rod dislocations that further dissociated to form trailing partial dislocations.

In the case of HCP materials, Qi et al. [131] reported that the plasticity at the vicinity of the void is driven predominantly by $\frac{1}{3}\langle \bar{1}100 \rangle$ partial dislocations on the basal plane and other unidentified dislocation structures. Tang et al. [123] studied the void growth and coalescence in single-crystal Mg and demonstrated that the evolution of the void shape and growth depends on the crystallographic orientation and size of the single crystal. In orientations that are favourable for twinning and contain a single void, twins originate from the void and grow laterally with increasing remote loading, leading to a flattening of the void. In the double void configuration, remote loading nucleates twins, which propagate to the end of the simulation box and grow laterally. Further loading nucleates another void at the intersection of the twin boundary, which grows at a higher rate, resulting in a rupture. In contrast, in orientations unfavourable for twinning with single voids, prismatic slip originates from the void surface after the formation of deformation bands at the initial strain levels, leading to the nucleation of another void. Similar mechanisms occur in the same orientations with two voids, wherein the prismatic slip originates from a void nucleating another void between the existing voids, leading to coalescence and then rupture.

The direction of macroscopic loading can lead to the shrinkage of existing voids. Xu et al. [132] studied nano-voids within a γ -TiAl matrix under uniaxial compression and reported three stages in the shrinkage process. In the first stage, i.e., elastic deformation, the void was shown to shrink along the loading direction while expanding in the transverse direction. In the second stage, the onset of plasticity caused the emission of partial dislocations and planar faults, which, in the third stage, propagated, interacted, and swapped through the entire system, resulting in void shrinkage. Similarly, Zhang et al. [133] investigated the void shrinkage in systems consisting of single and multiple voids. The emission of dislocations in a direction opposite to the applied load (e.g., dislocations on the upper side of the voids emitted towards the lower side and vice versa) led to material transport into the voids, which caused the voids to shrink. In addition, the density of the

Shockley partial dislocations and the shrinkage rate increased with the number of voids in the simulation box.

Several factors, including the temperature, strain rate, applied pressure, presence of other voids in the vicinity, size of voids, crystalline nature (single or polycrystal), grain size (in the case of polycrystals), and volume fraction of the precipitates, influence the rate of the nucleation and growth of voids. In their study, Yang et al. [134] reported that an increase in temperature and strain rate nucleated the voids earlier during the deformation, and the effect of the latter was more prominent than the former. While the effect of grain size had a negligible influence on the void volume fraction, larger grains nucleated more voids than that of smaller grains. Rawat and Raole [135] also had similar observations in BCC iron, wherein a higher strain rate nucleated more voids, while a lower strain rate resulted in a higher void volume fraction. This implies that nucleation is favoured at a higher strain rate, attributing the strain rate sensitivity to the formation of voids. Zhao et al. [120] also investigated the effect of temperature and stress on the void formation in FCC Al and demonstrated that the lattice-trapped delamination of the void nucleation was the rate-limiting process.

Cui et al. [117] studied the effect of Si precipitate size on the nucleation and growth of voids in a Cu matrix and reported that the onset of void nucleation (the initial delamination and dislocation emission stages) occurred early during the deformation for large precipitates compared to that of the smaller ones. In addition, the strain for the lattice delamination and dislocation-assisted delamination decreased with the strain rate. This indicates that the rate of the nucleation decreased with the strain rate, contrary to the findings reported elsewhere [135]. This may be the result of the difference in the strain rate sensitivity and/or the crystal structure of the material, both of which must be examined in depth.

The size of the void also influences the rate of growth. Several studies have shown that the stress required for dislocation emission from a void surface increases with a decrease in the void size [122,136]. This size effect is attributed to the starvation of dislocation sources with decreasing void sizes. Zhao and Liu [127] made similar observations and reported that the onset of void growth occurred at smaller strain levels for larger voids compared to those of smaller ones, as shown in Figure 6a. However, after the initiation of growth, the growth rate of the smaller voids was relatively higher than that of the larger voids (see the rate of growth in Figure 6a). In the case of multiple voids, their study suggests that the peak value of the stress triaxiality increased with the initial void ligament distance, reached a maximum, and then decreased with further increases in the ligament distance. Beyond the maxima, the void coalescence did not occur. Wang et al. [128] studied the effect of a Ni-Ni₃Al (γ/γ') interface on the rate of void growth and concluded that the growth rate was higher at the interface compared to that of a void located within both the Ni and Ni₃Al matrixes.

To date, it has been understood that the growth at the nanoscale occurs through material transport, which is facilitated by the emission of dislocations from the void surface. The nucleation of smaller voids occurs at higher strain levels compared to those of the larger ones. After the nucleation, the smaller voids grow at relatively higher rates (Figure 6a). However, in contradiction, the strain gradient formulations at higher length scales show that the larger voids grow at faster rates compared to those of the smaller ones [137,138]. In order to gain more insights, Segurado and Llorca [139] deployed a 2D dislocation dynamics-based formulation to understand the dislocation formation, interaction, and void growth. This study confirmed that the formation of more dislocations due to the availability of more sources at the vicinity of larger voids facilitated material transport and a higher rate of growth for larger voids compared to smaller voids (see Figure 6b). Chang et al. [21] extended this study by investigating the effect of void size on void growth in a 3D dislocation dynamics formulation and confirmed these conclusions (observe the higher rates of growth for larger voids in Figure 6b).

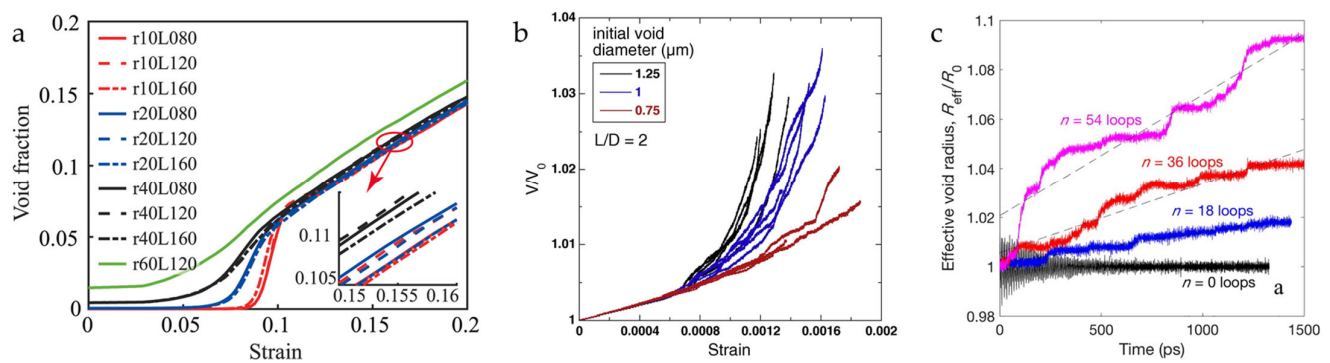


Figure 6. Effect of void size on rate of growth: (a) voids of nano-meter scale investigated using atomistic simulations. Observe that the rate of growth of smaller is greater than that of larger voids [128], (b) voids in micron scale studied using dislocation dynamics. In contrast to previous case, the rate of growth of larger voids is greater [21], and (c) the effect of plasticity at the void vicinity on its rate of growth. Note that the presence of more dislocation loops drives void growth [23]. (a) Reproduced with permission [128]. Copyright 2020, Elsevier. (b) Reproduced with permission [21]. Copyright 2015, Elsevier. (c) Reproduced under the terms of the CC-BY Creative Commons Attribution 4.0 International License [23].

Therefore, there appears to be a length-scale dependence on the type of physical mechanism that drives the void growth. Chang et al. [22] studied the growth in void sizes ranging from 1.5 nm to 100 nm using 2D atomistic simulations and observed the onset of plasticity by the dislocation emissions from the void surfaces in all the cases. However, the smaller voids (<10 nm) showed lower rates of growth than the larger ones, where the nucleation of the dislocations in the matrix facilitated the void growth. Recently, Sills and Boyce [23] studied void growth by introducing an increasing number of dislocation loops into the simulation box and observed that the rate of the void growth increased with the number of dislocation loops, as shown in Figure 6c. Therefore, Sills and Boyce suggested that this void growth is driven by the absorption of the dislocations generated during the plastic deformation in the matrix, instead of the dislocation emission at the void surface. Thus, in summary, it appears that void growth is driven by length-scale dependent physical mechanisms—the emission of dislocations from void surfaces in nano-meter length scales and the dislocation absorption occurring at higher length scales. Nevertheless, the contemporaneous occurrence of these mechanisms during plastic deformation remains elusive.

4.2. Mesoscale Crystal Plasticity Analyses of Voids

Typically, mesoscale physics-based numerical analyses are deployed to understand the effect of microstructure and loading conditions on the void growth in single crystals, bi-crystals, and polycrystals. In addition, there are a handful of studies (e.g., [140]) that have accounted for the mesoscale treatment of the nucleation and growth of voids in polycrystals, by implementing the classical models (e.g., GTN [14]) within the crystal plasticity framework. The void growth and coalescence at mesoscales are often related to extrinsic factors such as the stress states defined by the stress triaxiality and Lode parameter, loading conditions, and intrinsic factors such as the crystallographic orientations of the parent and neighbouring grains, the location of the voids relative to the grain boundaries, the phase boundaries, the triple junctions, and the void size.

The effect of the void size on its growth depends on the loading conditions. In their displacement-controlled loading conditions, Ha and Kim [141] demonstrated that the growth rate of the smaller voids was higher than that of the larger ones, as depicted in Figure 7a. In contrast, in several other studies based on stress-controlled loading conditions (e.g., [142]), larger voids were often associated with higher growth rates. In addition, it is commonly recognised that the effect of the crystallographic orientation on the void growth

rate also depends on the loading conditions, as illustrated in Figure 7b. For instance, in their seemingly stress-based loading conditions, Zhu et al. [143] reported a higher rate of void growth in hard orientations (i.e., unfavourable orientations for dislocation slip), while, in their strain-controlled loading conditions, Liu et al. [144] observed that a softer orientation supported a higher growth rate compared to that of the harder ones. Similar results were reported by Christodoulou et al. [145] (shown in Figure 7b) on the effect of the loading conditions (strain- and stress-controlled) on the relationship between the crystallographic orientation of the parent grain and the void growth in their fast Fourier-transforms-based crystal plasticity formulation.

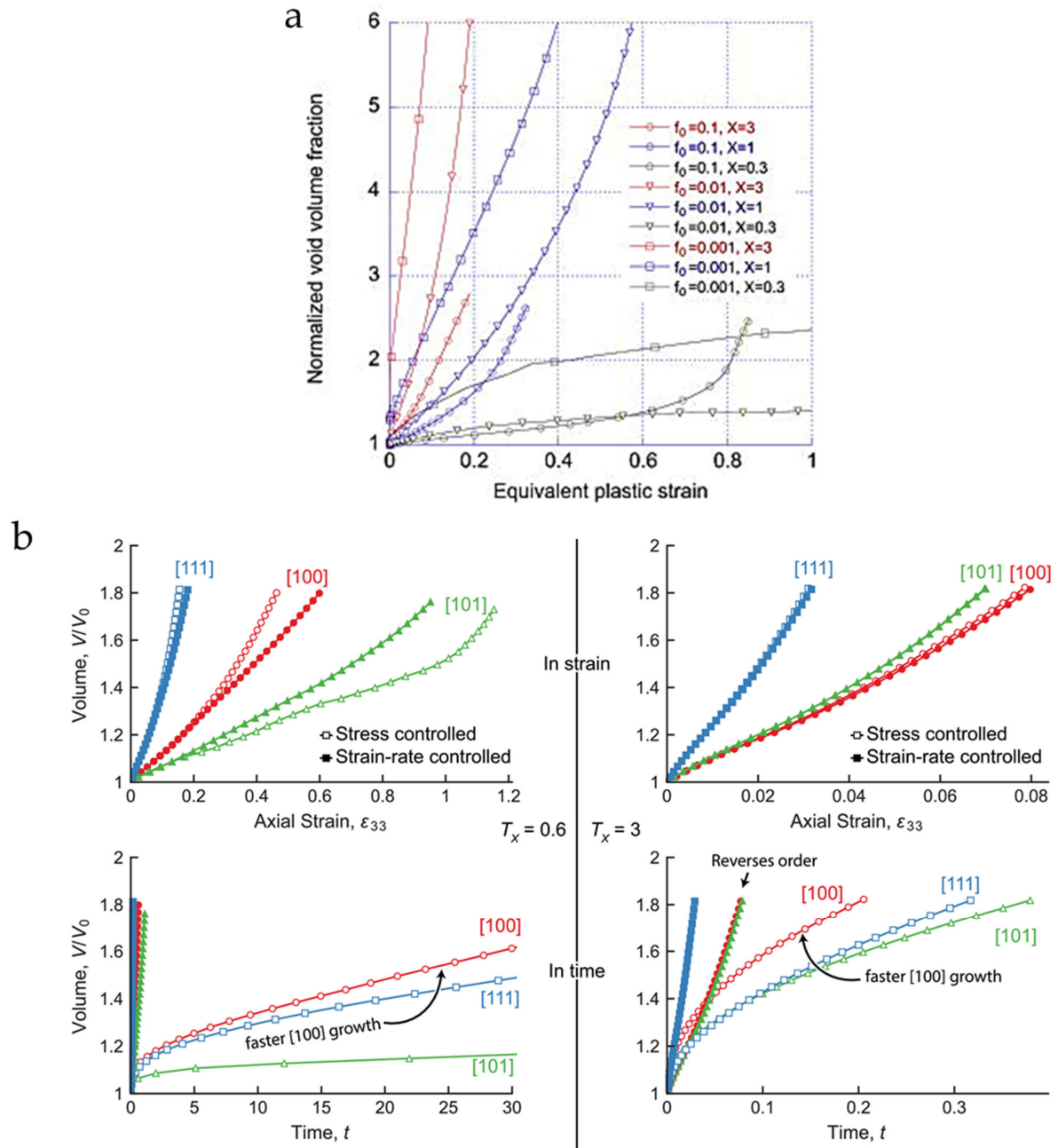


Figure 7. Effect of loading conditions on void growth showing: (a) displacement-controlled loading conditions, which seem to suggest that the smaller voids grow faster compared to the larger ones [141], and (b) the effect of loading conditions on growth of voids within parents of different crystallographic orientation [145]. (a) Reproduced with permission [141]. Copyright 2010, Elsevier. (b) Reproduced with permission [145]. Copyright 2021, Elsevier.

The growth rate of the voids in single crystals is influenced by their parent grain orientations. Several studies have demonstrated that the harder the orientation, the higher the rate of void growth, due to the accumulation of stresses at the void interface, which induces local plasticity [143,146–148]. This is applicable mostly at lower triaxialities, as the growth rates become less orientation-sensitive at higher triaxialities [143]. In addition, irrespective of crystallographic orientation, the growth rate of these voids increases with increasing stress triaxiality [141,149]. Furthermore, for a given orientation, the rate of void growth generally decreases with an increase in the Lode parameter at all the triaxialities [150]. Guo et al. [150] also showed that the void coalescence strain decreases with an increase in the triaxiality for a given Lode parameter (also see [147]).

Several studies have indicated that, for a given stress triaxiality, the rate of the void growth varies when placed within single crystal, bicrystal, and polycrystal representative volume elements (RVEs). The effect of these RVEs on the void growth in a few parent grain orientations is shown in Figure 8. Zhu et al. [143] demonstrated that, while the effect of a hard crystallographic orientation on the void growth was well preserved within all the RVEs (also see [151]), the rate of growth was highest in the single crystals compared to the other RVEs (see single crystals in Figure 8). In other words, the presence of neighbouring grains within polycrystals slows the rate of growth [145] (observe the rates of growth in polycrystal RVEs in Figure 8). This may not apply to all the orientations, since Zhu et al. [143] demonstrated that some single-crystal orientations with lower growth rates show higher growth rates in a polycrystalline setting. In addition, the growth rate within a given orientation is often influenced by its neighbouring orientations [146,152]. In the polycrystalline setting, the effect of neighbours is stronger in low triaxialities compared to that of high triaxialities [142]. However, Christodoulou et al. [145] suggested that the presence of hard neighbours leads to higher growth rates at higher triaxialities, irrespective of the orientation of the parent grain, while the effect of hard neighbours is minimal at lower triaxialities. These differences in conclusion may be caused by the nature of the RVEs considered in the respective studies. Dakshinamurthy et al. [148] found a significant effect of neighbouring grain orientations in the case of bicrystals (intergranular voids) at high triaxialities and showed that the presence of hard neighbours increases the growth rate within the parent grain.

The complex interactions between the texture, shape, and location of the voids influences the forming capability of the metals [153]. Jeong et al. [146] studied the growth rate of voids located at triple junctions and demonstrated that their orientation-specific growth rate behaviour (“harder the faster”) in single crystals no longer holds in the presence of neighbouring orientations (see Figure 8). This is suggested to be caused by the difference in the relative strengths of the parent and surrounding orientations. Similarly, Liu et al. [151] also suggested that the potential mode of failure at the void vicinity varies according to the relative strengths of the grains, driven by differences in the local plastic deformation. Furthermore, Liu et al. [151] also investigated the growth rate of voids located at grain boundaries and demonstrated that the mode of potential failure at the vicinity of the voids depended on the angle that the grain boundary made, with respect to the loading direction. While a grain boundary orientation of 0° leads to a transgranular fracture, a deviation to 45° , with respect to the loading direction, results in an intergranular failure at the void vicinity. Similarly, Asim et al. [154] showed that the growth rate of a void located at the interface of α - β phases in a titanium alloy increased with a decrease in the phase boundary inclination (PBI). In addition, the growth rate in the β (BCC) phase was found to be higher than that of the α (HCP) phase in the majority of the PBIs. In general, the anisotropic deformation behaviour of HCP materials, driven by local slip and deformation twinning systems, often results in complex shapes and growth rates of voids (e.g., see [155]).

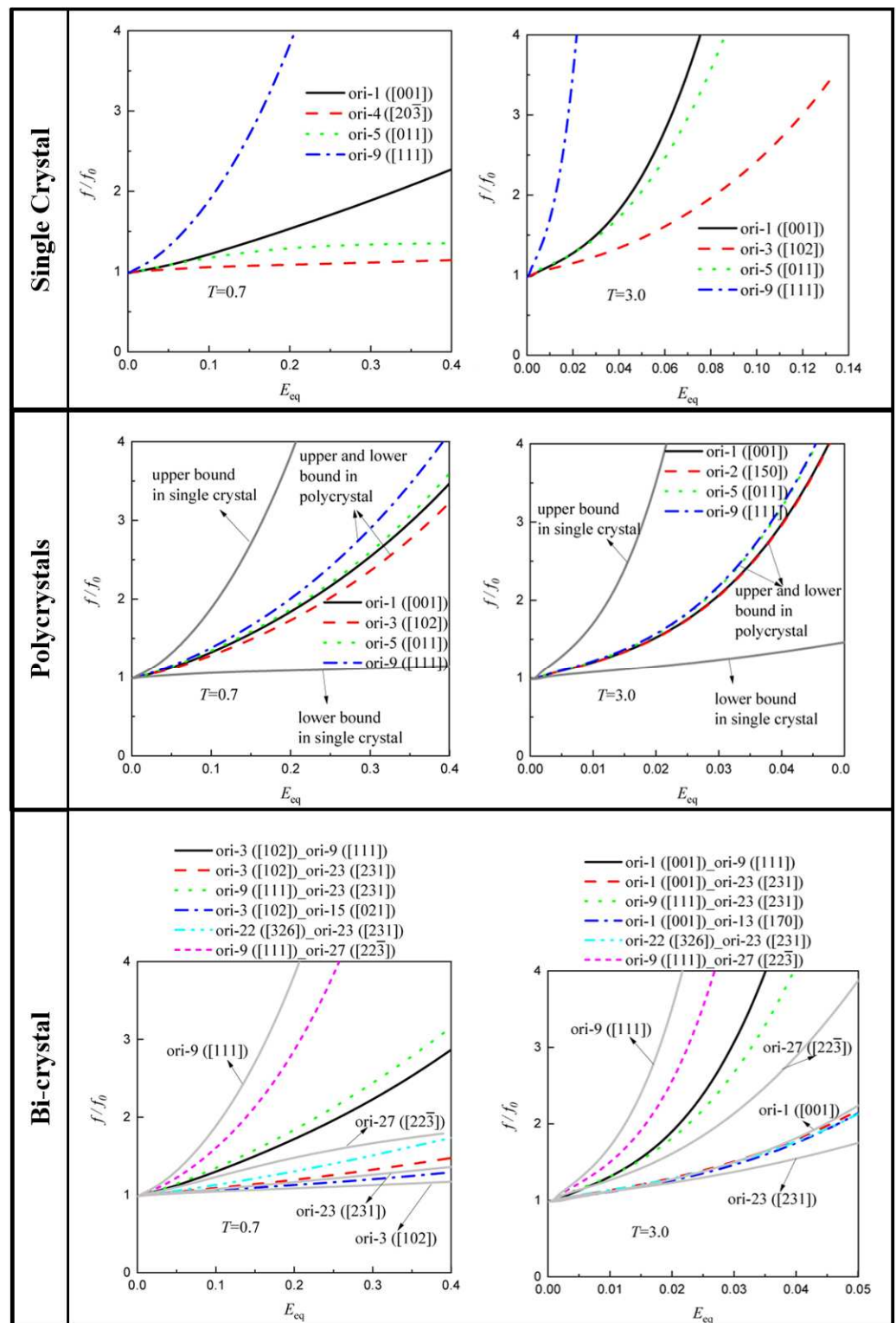


Figure 8. The evolution of growth of voids within a few selected parent grain orientations in single crystal, polycrystal, and bi-crystal representative volume elements. The trends in void growth observed in single crystals are not preserved in polycrystals and bi-crystals due to the presence of hard/soft neighbours. Reproduced with permission [143]. Copyright 2022, Elsevier.

5. Enhancement of Mechanical Properties by Hydrostatic Pressure

We have seen that the physical processes of void nucleation and growth are strongly correlated with the dislocation activities at the vicinity of voids. We know that forest

hardening raises the barrier to dislocation motion. An interesting question to ask is: can we take advantage of this to slow down void growth? It is well known that in an isotropic, homogeneous, and defect-free single crystal, the application of hydrostatic pressure does not generate shear stress and therefore will not deform the crystal. However, in real crystals, elastic discontinuities do exist, either through the non-uniform distribution of solutes, compressibility variations in non-cubic crystals, or the existence of precipitates and inclusions. These local discontinuities in the elastic properties provide various degrees of scaling between the local strain or dislocation activity with pressure, through one or more of the following mechanisms [156]:

1. A change in the shear modulus with pressure;
2. The generation of local shear stress at the elastic discontinuities;
3. An increase in the dislocation interaction energy and Peierls stress.

In the following, the effects of superimposed hydrostatic pressure on the plastic flow and ductility of various material systems are discussed. A comprehensive review is presented by Lewandowski and Lowhaphandu [157]. We introduce the essential points of reference [157] on plastic flow and ductility, together with some recent developments of the theories, which will form the foundation for our argument regarding the future perspectives of developments presented in Section 6.

5.1. Effects of Superimposed Pressure on Plastic Flow

Bridgeman's pioneering work [158,159] triggered considerable research interest into the effect of hydrostatic pressure on the flow and fracture behaviour of materials, as well as a series of models designed to explain and predict such behaviour. Spitzig and Richmond [160] demonstrated that the flow stress scales linearly with the superimposed hydrostatic pressure as:

$$\sigma = \sigma_0(1 + 3\alpha p) \quad (4)$$

where σ_0 is the the flow stress at 1 atm, p is the pressure, and α is a material-dependent pressure coefficient that was shown to be 20.0 Tpa^{-1} for iron-based materials and 56.5 for aluminium-based materials [160,161], highlighting that different materials respond to hydrostatic pressure differently.

According to Equation (4), superimposed hydrostatic stress increases the flow stress, as shown in Figure 9a. This increase is attributed to the pressure dependence of the shear modulus which, according to Jung [162], has the following form for edge and screw dislocations, respectively:

$$G' = G \left\{ 1 + \frac{p}{3} \left[\frac{1-v-2v^2}{1-v} \frac{1}{K} \left(\frac{dK}{dp} - 1 \right) + \frac{1-v+v^2}{1-v} \frac{2}{G} \left(\frac{dG}{dp} - \frac{G}{K} \right) + \frac{3}{G} \frac{dG}{dp} \right] \right\} (1 - \gamma p) \quad (5)$$

and

$$G' = G \left[1 + \frac{p}{G} \left(2 \frac{dG}{dp} - \frac{G}{K} \right) \right] (1 - \gamma p) \quad (6)$$

where G is the shear modulus at 1 atm, p is the imposed pressure, K is the bulk modulus, v is Poisson's ratio, and γ is the compressibility. It was argued that the pressure dependence of the shear modulus leads to the pressure dependence of the interaction force between the dislocations, and that it is such an increase in the interaction force that results in the annihilation of the dislocations or their escape to the free surface. This argument was used to explain the observation of a reduction in the dislocation density in Al and LiF crystals at a high pressure [163]. It was shown [162] that the pressure-induced change in the dislocation interaction force can be expressed by:

$$\Delta f_p^{int} = f_0^{int} k \quad (7)$$

where f_0^{int} is the interaction force at zero pressure and k is the pressure-dependent terms in Equation (5).

On the other hand, due to the dislocation migration volume, which is also referred to as transient dilatancy [164] and is a measure of the volumetric component of the activation volume tensor, additional work is required to account for the imposed pressure, and it is this additional work that gives rise to a raised Peierls barrier in the form [162]:

$$\Delta f_p^f = f_0^f \left[2 \frac{p}{G} \frac{dG}{dp} (1 - \gamma p) - \gamma p \right] \quad (8)$$

where f_0^f is the lattice friction force at zero pressure.

By comparing Equations (7) and (8) and using the elastic constants and pressure dependence of various monolithic metals, it was found that the magnitude of the lattice friction increases due to the pressure and completely balances the increase in the dislocation interaction force. Thus, the application of pressure does not increase the dislocation mobility. This point was confirmed by a molecular dynamic simulation [164], where a transient dilatation of $0.03 \text{ \AA}^3/\text{A}$ was reported for aluminium. This led to an 8 MPa increase in the Peierls stress at a 340 MPa imposed pressure. It is worth noting that, although the static dilatation, which arose due to the accumulation of dislocations and was possibly contributed to by the dilatational strain field, dislocation motion, or annihilation [165,166], was significantly higher (e.g., $6 \text{ \AA}^3/\text{A}$ in aluminium) than the transient dilatation, it did not contribute to the pressure dependence of the glide stress. Nevertheless, it was shown that this static dilatation is important when considering the interaction between the solute and dislocations [167].

Several dislocation-based models were proposed to account for the critical resolved shear stress required to activate the dislocation motion [162,168,169], among which the model put forward by Jung [162] possesses the following form:

$$\tau = \tau_0(1 - \gamma_0 p) \left(1 + \frac{2p}{G_0} \frac{dG}{dp} \right) \quad (9)$$

where τ and τ_0 are the critical resolved shear stresses at pressures p and 1 atm, respectively, and γ_0 is the compressibility at 1 atm, which was found to show the best agreement with the experiments [160,164]. Additionally, Equation (9) was found to be valid at extreme pressures tested up to 300 GPa by ramp release experiments [170,171] (although these tests were 1-D compression rather than pure hydrostatic).

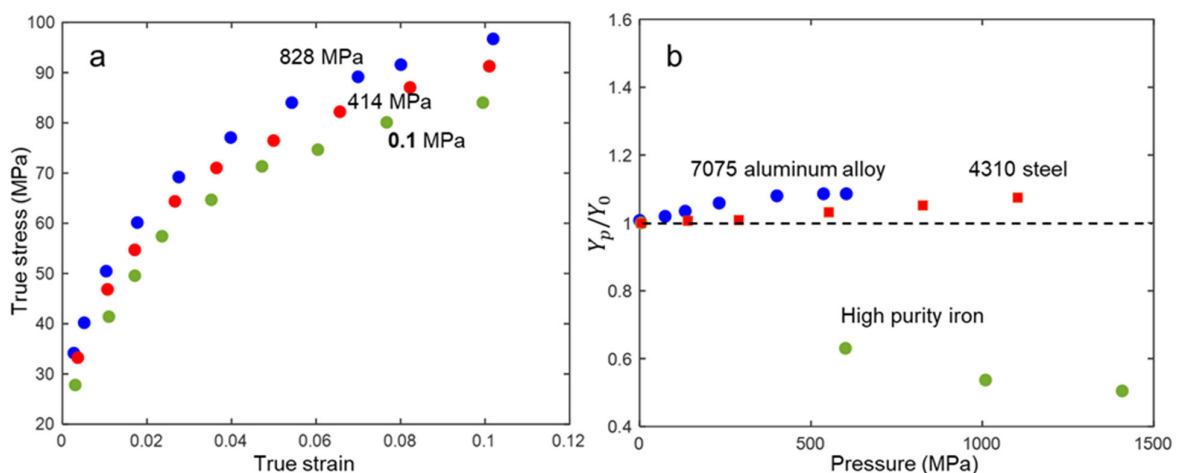


Figure 9. (a) The effect of superimposed hydrostatic pressure on the stress–strain response of a 1100 aluminium reproduced from reference [160]; and (b) the effect of superimposed hydrostatic pressure on the yield stress ratio (defined as the ratio between yield stress at pressure p and yield stress at 1 atm) for a 7075 aluminium alloy, 4310 steel, and high-purity iron, reproduced from [172–174] respectively.

It is noteworthy that the influence of the hydrostatic pressure on the yield stress in 7075 aluminium and 4310 steel (Figure 9b) was insignificant at the pressure range used. This trend reflects the general response of yield stress to pressure, according to the comprehensive survey by Lewandowski and Lowhaphandu [157]. The slight increase in the yield stress of these alloys was due to an increase in the Pielers stress, as mentioned above, and may be valid at low pressure ranges. At an extreme pressure (>10 GPa), the yield stress seemed to rise quite significantly with the pressure [171] (again, it is worth noting that the experiment in [171] was not purely hydrostatic). For high-purity iron, the yield strength seemed to decrease with the pressure, which is common in materials that deform initially via the Lüder's band and exhibit an upper yield point on their stress-strain curve [157]. Under hydrostatic pressure, the local chemical non-uniformities and inclusions in the materials lead to local shear stresses, causing the generation of mobile dislocations, which eliminate the yield point effect and reduce the yield strength [175,176]. This phenomenon was further demonstrated by the observation that the yield point effect returned upon subsequent annealing, as these mobile dislocations were re-locked by solute atoms [174,177].

In the above discussion, based on monolithic metals, it can be seen that hydrostatic pressure increases the flow stress but has a limited improvement on the yield stress at low pressure. As stated at the beginning of this section, the elastic discontinuities in these monolithic metals may not be significant enough (or the imposed pressure is not high enough) to bring about considerable dislocation hardening mechanisms, such that the yield stress would be considerably affected, although the pressure on the order of 1 GPa was evidenced to induce a noticeable enhancement of the flow stresses [160,173]. A more prominent effect of the hydrostatic pressure on the plastic flow is anticipated in metal matrix composites, as their reinforcing phases usually have different elastic constants. Ashby et al. [178] reported an analytical solution for a spherical particle embedded in an elastic isotropic matrix, and the maximum shear stress, τ_{max} , at the particle–matrix interface subjected to pressure p is given by:

$$\frac{\tau_{max}}{G_M} = - \left\{ \frac{3(K_M - K_P)}{K_M(3K_P + 4G_M)} \right\} p \quad (10)$$

where G_M is the shear modulus of the matrix and K_M and K_P are the bulk moduli of the matrix and the particle, respectively. The magnitude of the maximum shear stress depends on the difference in the bulk moduli, the decays with distance from the interface, and if the particle size is independent [179]. Though the maximum shear stress is independent of the particle size, the stress, hence the pressure, at which the dislocations are generated (i.e., the local shear stress exceeding the critical resolved shear stress) depends on the particle size and is shown to follow:

$$p_{crit} = Ar_0^n \quad (11)$$

where A is a constant and $n = 0.6 \pm 0.3$ [178]. The fact that the pressure-induced shear stress at the interface decays exponentially ($\propto r^{-3}$ [179]) indicates that the dislocations are generated locally at the interface, forming a dislocation shell encapsulating the particle. This is reflected by the TEM observation that only a fraction of SiO_2 , those of larger sizes, formed dislocation shells at a pressure of 2.5 GPa [178]. Note that Equation (11) is based on the assumption of spherical particles, whereas for those with irregular shapes, the local stress is higher at the same level of pressure [178].

As has been shown in previous studies, the yield stress increased by 50% for 1100 aluminium reinforced by 15 vol% of Al_2O_3 at a pressure of 1.8 GPa [157], 13% for 6016 aluminium reinforced by 15 vol% of Al_2O_3 at a pressure of 0.3 GPa [180], and 12% for 2014 aluminium reinforced by 20% SiC at a pressure of 0.7 GPa [181]. These improvements seem to be more significant compared to the 10% increase in the yield stress for monolithic metals, such as 7075 aluminium and 4310 steel at 0.6 GPa and 1.1 GPa, respectively (Figure 9b). The composites mentioned above have less than 20 vol% reinforcing particles. As the

dislocations generated by the hydrostatic pressure are locally distributed at the interface, it is anticipated that a more significant enhancement of the yield stress can be achieved by increasing the volume fraction of the particles, to an extent that the stress fields of the local dislocation shells start to overlap. However, studies on this point are scarce in the literature.

5.2. Effects of Superimposed Pressure on Plastic Flow

The processes of void nucleation and growth are the critical steps that lead to ductile fracture [10]. This process is facilitated by the development of internal hydrostatic tension during the deformation [20,182]. Thomason [183] has shown that the effective mean stress (the hydrostatic stress developed inside the samples as they deform), $\sigma_{m,eff}$, is modified by the superimposed hydrostatic pressure, by:

$$\sigma_{m,eff} = \sigma_m - P \quad (12)$$

where σ_m is the mean stress (i.e., the hydrostatic pressure $(\sigma_1 + \sigma_2 + \sigma_3)/3$) and P is the magnitude of the superimposed pressure. This condition leads to the following void nucleation criteria:

$$\varepsilon_n = Kr_p(\sigma_c - \sigma_m + P)^2 \quad (13)$$

for particles smaller than 1 μm [184], and

$$\sigma_c = \sigma_m + \bar{\sigma} + P \quad (14)$$

for particles bigger than 1 μm [185], where ε_n and σ_c are the critical strain and stress for nucleating voids, respectively, K is a constant depending on the volume fraction of the particles, r_p is the particle radius, σ_c is the critical interface cohesive strength, and $\bar{\sigma}$ is the effective stress. It is immediately apparent that the superimposed pressure counters the internal hydrostatic tension and raises the critical stress/strain for void nucleation.

As we discussed above, the mechanical growth of voids is physically realised by the glide of dislocations, and a proper level of hydrostatic pressure creates dislocation shells encapsulating the void-nucleating particles. It is therefore reasonable to speculate that hydrostatic pressure can enhance the ductility of particle-containing materials by one or more of the following mechanisms:

1. Dislocation shells encapsulating the voids nucleated from particles serve as barriers for the dislocations gliding away from the void surfaces. Therefore, the void growth rate could be delayed;
2. Hydrostatic stress increases the Peierls stress and dislocation interaction energy, generating additional barriers for the dislocation glide, hence resulting in void growth;
3. Superimposed hydrostatic pressure counters the hydrostatic tension inside the deforming body.

Such anticipated enhancements of the ductility of particle-reinforced composites are demonstrated in Figure 10, where the enhancement of the ductility via superimposed hydrostatic pressure is remarkable. These enhancements could be attributed to the aforementioned mechanisms that inhibit void nucleation and growth. Earlier experimental and computational studies have also demonstrated that, after deformation under superimposed hydrostatic pressure, the void volume fraction was reduced [186–188].

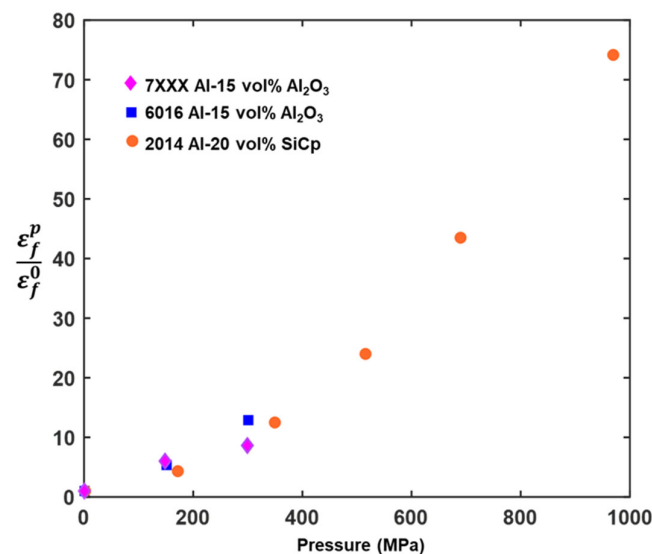


Figure 10. The effect of superimposed hydrostatic pressure on the fracture strain ratio, defined as the ratio between the fracture strain at applied pressure p , (ϵ_f^p), and that at atmospheric pressure (ϵ_f^0). Graph reproduced based on data available in [181,188,189].

Apart from enhancing strength and ductility, an added benefit of superimposed hydrostatic pressure arises from the inhibition of void nucleation during heat treatment. In the case of significantly differing thermal expansion coefficients between the inclusions and matrix, strong radial tension may lead to interface delamination and therefore void nucleation. Superimposed hydrostatic pressure is assumed to reduce or eliminate such adverse effects and retain structural integrity after heat treatment.

6. Summary and Future Directions

In this article, we reviewed the common techniques for detecting voids in deforming or deformed bodies in Section 2. Ultrasonic and acoustic emission techniques are probably the most suitable for the online monitoring of void evolution in industrial settings, given their underlying principles of application. In Sections 3 and 4, the theories on ductile fracture were reviewed, highlighting the knowledge gap between stress triaxiality and the physical processes of mechanical void nucleation and growth. Such knowledge is essential for designing material properties from the first principles. In Section 5, the effects of superimposed hydrostatic pressure on the plastic flow and fracture of metallic materials were discussed, complementing the previous sections. We conclude that superimposed hydrostatic pressure can enhance the yield strength moderately and the fracture strain significantly. This can be fundamentally attributed to the generation of dislocations at the elastic discontinuities (e.g., reinforcing particles in composites) that interact with the dislocation activity and consequently slow down the void growth. Such beneficial effects have been exploited in various forming processes [190–192] to enhance the forming efficiency and formability of materials that would otherwise be difficult-to-form.

In light of the previous research on the effects of hydrostatic pressure, we suggest that this field can be advanced in multiple ways. The majority of previous publications in this field have focused on the effects of superimposed pressure. The limitations of these previous works are twofold: first, although the outputs from these studies have been integrated into the development of forming processes, it is arguable that the service conditions of materials or components are often not hydrostatic. Furthermore, if hydrostatic forming is followed by heat treatment, the dislocation structures responsible for the property enhancement may be removed. Therefore, a part of the efforts should be devoted to pre-pressurization. Based on the existing literature, we detailed three mechanisms for this property enhancement by deforming materials under hydrostatic pressure at the beginning of Section 5. Here,

we propose three mechanisms by which this pre-pressurization may provide property enhancement:

1. Dislocation shells form around the hetero-phase particles under pre-pressurization, which can further enhance the Orowan mechanisms;
2. The dislocation shells increase the effective range of the back stresses between the heterophases [193];
3. The work-hardening capacity of the matrix materials is preserved after pre-pressurization.

The above proposition may potentially support hydrostatic pre-pressurization as a potential method for increasing strength and ductility simultaneously.

Second, the existing studies fall short of sufficiently covering how the partitioning of the hydrostatic and deviatoric parts of the stress components during pressure soaking or pressurization would affect the mechanical properties of the sample. This concern arises from the fact that ensuring a perfect hydrostatic environment is difficult during experimental processing and especially a problem during industrial manufacturing, such as hydrostatic extrusion, where deviatoric stress is necessary to bring the component into shape. Therefore, questions arise regarding how the mechanical properties would differ between pre-pressurization and deformation under pressure, and how hydrostatic-deviatoric stress partitioning affects mechanical property enhancement. These questions point to the future directions of the research that is necessary for developing such a treatment into a fully integrated manufacturing tool for high-performance components. Based on the current status of the experimental techniques available, in situ hydrostatic pressurization studies under synchrotron radiation are perhaps the most suitable solution to the hydrostatic-deviatoric partitioning problem, and data from such experiments are valuable for calibrating the appropriate constitutive relationships that can be integrated into manufacturing simulations to guide production.

In addition to the above-mentioned concerns, there are a number of other questions relating to the impact of this treatment's efficacy that should be addressed in future research. Thus, future studies should focus on determining the hydrostatic pressure sensitivity (in terms of the dislocation generation) of a particular material system and the temperature at which the pressure is applied, the interaction between the dislocation shell and the void nucleation and growth, and the size, shape, and volume fraction of the heterophases. Although the industrial application of a pre-pressurization higher than 1 GPa seems difficult at the moment, laboratory research may help to facilitate the future realization of such a processing industry.

Author Contributions: Y.G. and E.A. drafted the introduction; Y.G. drafted Sections 2, 5 and 6; E.A. drafted Section 3; C.P. drafted Section 4. All authors edited and reviewed the paper. All authors have read and agreed to the published version of the manuscript.

Funding: This research was funded by National Natural Science Foundation of China, grant number 52201149 and National Science and Technology Major Project, grant number J2019-VI-0019-0134.

Data Availability Statement: No new data were created or analysed in this study. Data sharing is not applicable to this article.

Conflicts of Interest: The authors declare no conflict of interest. The funders had no role in the design of the study; in the collection, analyses, or interpretation of data; in the writing of the manuscript; or in the decision to publish the results.

References

1. Leclerc, J.; Marteleur, M.; Colla, M.-S.; Pardoën, T.; Noels, L.; Nguyen, V.-D. Ductile Fracture of High Strength Steels with Morphological Anisotropy, Part II: Nonlocal Micromechanics-Based Modeling. *Eng. Fract. Mech.* **2021**, *248*, 107716. [[CrossRef](#)]
2. Bonora, N.; Testa, G. Plasticity Damage Self-Consistent Model Incorporating Stress Triaxiality and Shear Controlled Fracture Mechanisms—Model Formulation. *Eng. Fract. Mech.* **2022**, *271*, 108634. [[CrossRef](#)]
3. Benzerga, A.A.; Leblond, J.-B.; Needleman, A.; Tvergaard, V. Ductile Failure Modeling. *Int. J. Fract.* **2016**, *201*, 29–80. [[CrossRef](#)]
4. Pineau, A.; Benzerga, A.A.; Pardoën, T. Failure of Metals I: Brittle and Ductile Fracture. *Acta Mater.* **2016**, *107*, 424–483. [[CrossRef](#)]
5. Tipper, C.F. The Fracture of Metals. *Metallurgia* **1949**, *39*, 133–137.

6. Goods, S.H.; Brown, L.M. Overview No. 1: The Nucleation of Cavities by Plastic Deformation. *Acta Metall.* **1979**, *27*, 1–15. [[CrossRef](#)]
7. Das, A.; Kumar Chakravartty, J. Fractographic Correlations with Mechanical Properties in Ferritic Martensitic Steels. *Surf. Topogr.* **2017**, *5*, 045006. [[CrossRef](#)]
8. Curran, D.R.; Seaman, L.; Shockey, D.A. Dynamic Failure of Solids. *Phys. Rep.* **1987**, *147*, 253–388. [[CrossRef](#)]
9. Anderson, T.L. *Fracture Mechanics*; CRC Press: Boca Raton, FL, USA, 2017; ISBN 9781315370293.
10. Pineau, A.; Pardoën, T. Failure of Metals. In *Comprehensive Structural Integrity*; Milne, I., Ritchie, R.O., Karihaloo, B., Eds.; Pergamon: Oxford, UK, 2007; pp. 684–797.
11. Wciślik, W.; Lipiec, S. Void-Induced Ductile Fracture of Metals: Experimental Observations. *Materials* **2022**, *15*, 6473. [[CrossRef](#)]
12. Das, A.; Das, S.K.; Sivaprasad, S.; Tarafder, M.; Tarafder, S. Analysis of Damage Accumulations in High Strength Low Alloy Steels under Monotonic Deformation. *Procedia Eng.* **2013**, *55*, 786–792. [[CrossRef](#)]
13. Gurson, A.L. Continuum Theory of Ductile Rupture by Void Nucleation and Growth: Part I—Yield Criteria and Flow Rules for Porous Ductile Media. *J. Eng. Mater. Technol.* **1977**, *99*, 2–15. [[CrossRef](#)]
14. Tvergaard, V.; Needleman, A. Analysis of the Cup-Cone Fracture in a Round Tensile Bar. *Acta Metall.* **1984**, *32*, 157–169. [[CrossRef](#)]
15. Leblond, J.B.; Perrin, G.; Suquet, P. Exact Results and Approximate Models for Porous Viscoplastic Solids. *Int. J. Plast.* **1994**, *10*, 213–235. [[CrossRef](#)]
16. Benzerga, A.A.; Besson, J. Plastic Potentials for Anisotropic Porous Solids. *Eur. J. Mech.—A/Solids* **2001**, *20*, 397–434. [[CrossRef](#)]
17. Thomason, P.F. A Three-Dimensional Model for Ductile Fracture by the Growth and Coalescence of Microvoids. *Acta Metall.* **1985**, *33*, 1087–1095. [[CrossRef](#)]
18. Siruguet, K.; Leblond, J.-B. Effect of Void Locking by Inclusions upon the Plastic Behavior of Porous Ductile Solids—I: Theoretical Modeling and Numerical Study of Void Growth. *Int. J. Plast.* **2004**, *20*, 225–254. [[CrossRef](#)]
19. Siruguet, K.; Leblond, J.-B. Effect of Void Locking by Inclusions upon the Plastic Behavior of Porous Ductile Solids—Part II: Theoretical Modeling and Numerical Study of Void Coalescence. *Int. J. Plast.* **2004**, *20*, 255–268. [[CrossRef](#)]
20. Xu, Z.; Britton, B.; Guo, Y. Casting Voids in Nickel Superalloy and the Mechanical Behaviour under Room Temperature Tensile Deformation. *Mater. Sci. Eng. A* **2021**, *806*, 140800. [[CrossRef](#)]
21. Chang, H.-J.; Segurado, J.; LLorca, J. Three-Dimensional Dislocation Dynamics Analysis of Size Effects on Void Growth. *Scr. Mater.* **2015**, *95*, 11–14. [[CrossRef](#)]
22. Chang, H.J.; Segurado, J.; De La Fuente, O.R.; Pabón, B.M.; LLorca, J. Molecular Dynamics Modeling and Simulation of Void Growth in Two Dimensions. *Model. Simul. Mat. Sci. Eng.* **2013**, *21*, 75010. [[CrossRef](#)]
23. Sills, R.B.; Boyce, B.L. Void Growth by Dislocation Adsorption. *Mater. Res. Lett.* **2020**, *8*, 103–109. [[CrossRef](#)]
24. Segurado, J.; LLorca, J. Discrete Dislocation Dynamics Analysis of the Effect of Lattice Orientation on Void Growth in Single Crystals. *Int. J. Plast.* **2010**, *26*, 806–819. [[CrossRef](#)]
25. Guo, Y.; Zong, C.; Britton, T.B. Development of Local Plasticity around Voids during Tensile Deformation. *Mater. Sci. Eng. A* **2021**, *814*, 141227. [[CrossRef](#)]
26. Lubarda, V.A.; Schneider, M.S.; Kalantar, D.H.; Remington, B.A.; Meyers, M.A. Void Growth by Dislocation Emission. *Acta Mater.* **2004**, *52*, 1397–1408. [[CrossRef](#)]
27. Lubarda, V.A. Image Force on a Straight Dislocation Emitted from a Cylindrical Void. *Int. J. Solids Struct.* **2011**, *48*, 648–660. [[CrossRef](#)]
28. Gungor, M.R.; Maroudas, D.; Zhou, S. Molecular-Dynamics Study of the Mechanism and Kinetics of Void Growth in Ductile Metallic Thin Films. *Appl. Phys. Lett.* **2000**, *77*, 343–345. [[CrossRef](#)]
29. Ahn, D.C.; Sofronis, P.; Minich, R. On the Micromechanics of Void Growth by Prismatic-Dislocation Loop Emission. *J. Mech. Phys. Solids* **2006**, *54*, 735–755. [[CrossRef](#)]
30. Le Roy, G.; Edwards, G.; Ashby, M.F. A Model of Ductile Fracture Based on the Nucleation and Growth of Voids. *Acta Metall.* **1981**, *29*, 1509–1522. [[CrossRef](#)]
31. Pardoën, T.; Delannay, F. On the Coalescence of Voids in Prestrained Notched Round Copper Bars. *Fatigue Fract. Eng. Mater. Struct.* **1998**, *21*, 1459–1472. [[CrossRef](#)]
32. Lemaitre, J.; Dufailly, J. Damage Measurements. *Eng. Fract. Mech.* **1987**, *28*, 643–661. [[CrossRef](#)]
33. Bonora, N.; Ruggiero, A.; Gentile, D.; de Meo, S. Practical Applicability and Limitations of the Elastic Modulus Degradation Technique for Damage Measurements in Ductile Metals. *Strain* **2011**, *47*, 241–254. [[CrossRef](#)]
34. Lio Alves, M.; Yu, J.; Jones, N. On the Elastic Modulus Degradation in Continuum Damage Mechanics. *Comput. Struct.* **2000**, *76*, 703–712. [[CrossRef](#)]
35. Guelorget, B.; François, M.; Lu, J. Microindentation as a Local Damage Measurement Technique. *Mater. Lett.* **2007**, *61*, 34–36. [[CrossRef](#)]
36. Tasan, C.C.; Hoefnagels, J.P.M.; Geers, M.G.D. Identification of the Continuum Damage Parameter: An Experimental Challenge in Modeling Damage Evolution. *Acta Mater.* **2012**, *60*, 3581–3589. [[CrossRef](#)]
37. Nagarajan, A. Ultrasonic Study of Elasticity-Porosity Relationship in Polycrystalline Alumina. *J. Appl. Phys.* **1971**, *42*, 3693–3696. [[CrossRef](#)]
38. Jeong, H.; Hsus, D.K. Quantitative Estimation of Material Properties of Porous Ceramics by Means of Composite Micromechanics and Ultrasonic Velocity. *NDT&E Int.* **1996**, *29*, 95–101.

39. Augereau, F.; Roque, V.; Robert, L.; Despaux, G. Non-Destructive Testing by Acoustic Signature of Damage Level in 304L Steel Samples Submitted to Rolling, Tensile Test and Thermal Annealing Treatments. *Mater. Sci. Eng.* **1999**, *266*, 285–294. [[CrossRef](#)]
40. Yeh, H.Y.; Cheng, J.H. NDE of Metal Damage: Ultrasonics with a Damage Mechanics Model. *Int. J. Solids Struct.* **2003**, *40*, 7285–7298. [[CrossRef](#)]
41. Dattoma, V.; Nobile, R.; Panella, F.W.; Saponaro, A. Real-Time Monitoring of Damage Evolution by Nonlinear Ultrasonic Technique. *Procedia Struct. Integr.* **2019**, *24*, 583–592. [[CrossRef](#)]
42. Zhang, S.; Zhang, S.; Wang, B.; Habetler, T.G. Deep Learning Algorithms for Bearing Fault Diagnostics—A Comprehensive Review. *IEEE Access* **2020**, *8*, 29857–29881. [[CrossRef](#)]
43. Cook, O.; Huang, N.; Smithson, R.; Kube, C.; Beese, A.; Argüelles, A. Ultrasonic Characterization of Porosity in Components Made by Binder Jet Additive Manufacturing. *Mater. Eval.* **2022**, *80*, 37–44. [[CrossRef](#)]
44. Foster, D.R.; Dapino, M.J.; Babu, S.S. Elastic Constants of Ultrasonic Additive Manufactured Al 3003-H18. *Ultrasonics* **2013**, *53*, 211–218. [[CrossRef](#)] [[PubMed](#)]
45. Lopez, A.; Bacelar, R.; Pires, I.; Santos, T.G.; Sousa, J.P.; Quintino, L. Non-Destructive Testing Application of Radiography and Ultrasound for Wire and Arc Additive Manufacturing. *Addit. Manuf.* **2018**, *21*, 298–306. [[CrossRef](#)]
46. Koester, L.W.; Taheri, H.; Bigelow, T.A.; Collins, P.C. Nondestructive Testing for Metal Parts Fabricated Using Powder-Based Additive Manufacturing In-Situ Process Monitoring and NDE for Additive Manufacturing View Project. *Mater. Eval.* **2018**, *76*, 514–524.
47. Ashby, M.F. Work Hardening of Dispersion-Hardened Crystals. *Philos. Mag.* **1966**, *14*, 1157–1178. [[CrossRef](#)]
48. Tanaka, K.; Mori, T.; Nakamura, T. Cavity Formation at the Interface of a Spherical Inclusion in a Plastically Deformed Matrix. *Philos. Mag.* **1970**, *21*, 267–279. [[CrossRef](#)]
49. Carpenter, S.H.; Higgins, F.P. Sources of Acoustic Emission Generated During the Plastic Deformation of 7075 Aluminum Alloy. *Metall. Trans. A* **1977**, *8*, 1629–1632. [[CrossRef](#)]
50. Drozdenko, D.; Bohlen, J.; Yi, S.; Minárik, P.; Chmelík, F.; Dobroň, P. Investigating a Twinning–Detwinning Process in Wrought Mg Alloys by the Acoustic Emission Technique. *Acta Mater.* **2016**, *110*, 103–113. [[CrossRef](#)]
51. Richeton, T.; Weiss, J.; Louchet, F. Breakdown of Avalanche Critical Behaviour in Polycrystalline Plasticity. *Nat. Mater.* **2005**, *4*, 465–469. [[CrossRef](#)]
52. Vinogradov, A.; Yasnikov, I.S.; Estrin, Y. Stochastic Dislocation Kinetics and Fractal Structures in Deforming Metals Probed by Acoustic Emission and Surface Topography Measurements. *J. Appl. Phys.* **2014**, *115*, 233506. [[CrossRef](#)]
53. Kahirdeh, A.; Sauerbrunn, C.; Modarres, M. Acoustic Emission Entropy as a Measure of Damage in Materials. *AIP Conf. Proc.* **2016**, *1757*, 060007.
54. Holford, K.M.; Pullin, R.; Evans, S.L.; Eaton, M.J.; Hensman, J.; Worden, K. Acoustic Emission for Monitoring Aircraft Structures. *Proc. Inst. Mech. Eng. G J. Aerosp. Eng.* **2009**, *223*, 525–532. [[CrossRef](#)]
55. Grondel, Â.; Delebarre, C.; Assaad, J.; Dupuis, J.-P.; Reithler, L. Fatigue Crack Monitoring of Riveted Aluminium Strap Joints by Lamb Wave Analysis and Acoustic Emission Measurement Techniques. *NDT&E Int.* **2002**, *35*, 137–146.
56. Manson, G.; Worden, K.; Holford, K.; Pullin, R. Visualisation and Dimension Reduction of Acoustic Emission Data for Damage Detection. *J. Intell. Mater. Syst. Struct.* **2001**, *12*, 529–536. [[CrossRef](#)]
57. Mummery, P.M.; Derby, B.; Scruby, C.B. Acoustic emission from particulate-reinforced metal matrix composites. *Acta Metall. Mater.* **1993**, *41*, 1431–1445. [[CrossRef](#)]
58. Rabiei, M.; Modarres, M. Quantitative Methods for Structural Health Management Using in Situ Acoustic Emission Monitoring. *Int. J. Fatigue* **2013**, *49*, 81–89. [[CrossRef](#)]
59. Dunegan, H.; Harris, D. Acoustic Emission—a New Nondestructive Testing Tool. *Ultrasonics* **1969**, *7*, 160–166. [[CrossRef](#)]
60. Dobroň, P.; Bohlen, J.; Chmelík, F.; Lukáč, P.; Letzig, D.; Kainer, K.U. Acoustic Emission during Stress Relaxation of Pure Magnesium and AZ Magnesium Alloys. *Mater. Sci. Eng. A* **2007**, *462*, 307–310. [[CrossRef](#)]
61. Lazarev, A.; Vinogradov, A. About plastic instabilities in iron and power spectrum of acoustic emission. *J. Acoust. Emiss.* **2009**, *27*, 144–156.
62. Scruby, C.; Wadley, H.; Sinclair, J.E. The Origin of Acoustic Emission during Deformation of Aluminium and an Aluminium–Magnesium Alloy. *Philos. Mag. A Phys. Condens. Matter Struct. Defects Mech. Prop.* **1981**, *44*, 249–274. [[CrossRef](#)]
63. Sedgwick, R.T. Acoustic Emission from Single Crystals of LiF and KCl. *J. Appl. Phys.* **1968**, *39*, 1728–1740. [[CrossRef](#)]
64. James, D.R.; Carpenter, S.H. Relationship between Acoustic Emission and Dislocation Kinetics in Crystalline Solids. *J. Appl. Phys.* **1971**, *42*, 4685–4697. [[CrossRef](#)]
65. Fisher, R.M.; Lally, J.S. Microplasticity detected by an acoustic technique. *Can. J. Phys.* **1967**, *45*, 1147–1159. [[CrossRef](#)]
66. Imanaka, T.; Sano, K.; Shimizu, M. Dislocation Attenuation and Acoustic Emission during Deformation in Copper Single Crystals. *Cryst. Lattice Defects* **1973**, *4*, 57–64.
67. Scruby, C.B.; Wadley, H.N.G.; Rusbridge, K.; Stockham-Jones, D. Influence of Microstructure on Acoustic Emission during Deformation of Aluminium Alloys. *Met. Sci.* **1981**, *15*, 599–608. [[CrossRef](#)]
68. Natsik, V.D.; Burkanov, A.N. Radiation of Rayleigh Waves by an Edge Dislocation Emerged on Crystal Surface. *Fizika Tverdogo Tela* **1972**, *14*, 1289.
69. Kiesewetter, N. Acoustic Emission from Moving Dislocations. *Scr. Metall.* **1974**, *8*, 249–252. [[CrossRef](#)]
70. Natsik, V.D.; Chishko, K.A. Dynamics and Sound Radiation of Dislocation Frank-Read Source. *Fiz. Tverd.* **1975**, *17*, 342–345.

71. Vinogradov, A.Y.; Merson, D.L. The Nature of Acoustic Emission during Deformation Processes in Metallic Materials. *Low Temp. Phys.* **2018**, *44*, 930–937. [[CrossRef](#)]
72. Merson, D.; Nadtochiy, M.; Patlan, V.; Vinogradov, A.; Kitagawa, I.S. On the Role of Free Surface in Acoustic Emission. *Mater. Sci. Eng. A* **1997**, *234–236*, 587–590. [[CrossRef](#)]
73. Vinogradov, A.; Yasnikov, I.S.; Merson, D.L. Phenomenological Approach towards Modelling the Acoustic Emission Due to Plastic Deformation in Metals. *Scr. Mater.* **2019**, *170*, 172–176. [[CrossRef](#)]
74. Van Liempt, P. Materials Processing Technology Workhardening and Substructural Geometry of Metals. *Process. Technol.* **1994**, *45*, 459–464. [[CrossRef](#)]
75. Hollang, L.; Hieckmann, E.; Brunner, D.; Holste, C.; Skrotzki, W. Scaling Effects in the Plasticity of Nickel. *Mater. Sci. Eng. A* **2006**, *424*, 138–153. [[CrossRef](#)]
76. Zhao, P.; Sun, Y.; Jiao, J.; Fang, G. Correlation between Acoustic Emission Detection and Microstructural Characterization for Damage Evolution. *Eng. Fract. Mech.* **2020**, *230*, 106967. [[CrossRef](#)]
77. Guo, Y.; Schwiedrzik, J.; Michler, J.; Maeder, X. On the Nucleation and Growth of $\{112\bar{2}\}$ Twin in Commercial Purity Titanium: In Situ Investigation of the Local Stress Field and Dislocation Density Distribution. *Acta Mater.* **2016**, *120*, 292–301. [[CrossRef](#)]
78. Pürstl, J.T.; Jones, H.O.; Edwards, T.E.J.; Thompson, R.P.; Di Gioacchino, F.; Jones, N.G.; Clegg, W.J. On the Extraction of Yield Stresses from Micro-Compression Experiments. *Mater. Sci. Eng. A* **2021**, *800*, 140323. [[CrossRef](#)]
79. Ciaburro, G.; Iannace, G. Machine-Learning-Based Methods for Acoustic Emission Testing: A Review. *Appl. Sci.* **2022**, *12*, 10476. [[CrossRef](#)]
80. Pomponi, E.; Vinogradov, A. A Real-Time Approach to Acoustic Emission Clustering. *Mech. Syst. Signal Process.* **2013**, *40*, 791–804. [[CrossRef](#)]
81. Shevchik, S.A.; Kenel, C.; Leinenbach, C.; Wasmer, K. Acoustic Emission for in Situ Quality Monitoring in Additive Manufacturing Using Spectral Convolutional Neural Networks. *Addit. Manuf.* **2018**, *21*, 598–604. [[CrossRef](#)]
82. Withers, P.J.; Bouman, C.; Carmignato, S.; Cnudde, V.; Grimaldi, D.; Hagen, C.K.; Maire, E.; Manley, M.; du Plessis, A.; Stock, S.R. X-Ray Computed Tomography. *Nat. Rev. Methods Prim.* **2021**, *1*, 18. [[CrossRef](#)]
83. Feldkamp, L.A.; Davis, L.C.; Kress, J.W. Practical Cone-Beam Algorithm. *J. Opt. Soc. Am. A* **1984**, *1*, 612–619. [[CrossRef](#)]
84. Maire, E.; Withers, P.J. Quantitative X-ray Tomography. *Int. Mater. Rev.* **2014**, *59*, 1–43. [[CrossRef](#)]
85. Daly, M.; Burnett, T.L.; Pickering, E.J.; Tuck, O.C.G.; Léonard, F.; Kelley, R.; Withers, P.J.; Sherry, A.H. A Multi-Scale Correlative Investigation of Ductile Fracture. *Acta Mater.* **2017**, *130*, 56–68. [[CrossRef](#)]
86. Jia, L.-J.; Zhang, R.; Zhou, C.-F.; Gu, T.-Y.; Liu, T.; Xie, J.-B.; He, M.-C.; Xia, M.; Chen, B. In-Situ Three-Dimensional X-ray Investigation on Micro Ductile Fracture Mechanism of a High-Mn Steel with Delayed Necking Effect. *J. Mater. Res. Technol.* **2023**, *24*, 1076–1087. [[CrossRef](#)]
87. Depraetere, R.; De Waele, W.; Cauwels, M.; Depover, T.; Verbeken, K.; Boone, M.; Hertelé, S. Influence of Stress Triaxiality on Hydrogen Assisted Ductile Damage in an X70 Pipeline Steel. *Mater. Sci. Eng. A* **2023**, *864*, 144549. [[CrossRef](#)]
88. Toda, H.; Takijiri, A.; Azuma, M.; Yabu, S.; Hayashi, K.; Seo, D.; Kobayashi, M.; Hirayama, K.; Takeuchi, A.; Uesugi, K. Damage Micromechanisms in Dual-Phase Steel Investigated with Combined Phase- and Absorption-Contrast Tomography. *Acta Mater.* **2017**, *126*, 401–412. [[CrossRef](#)]
89. Ludwig, W.; Reischig, P.; King, A.; Herbig, M.; Lauridsen, E.M.; Johnson, G.; Marrow, T.J.; Buffire, J.Y. Three-Dimensional Grain Mapping by x-Ray Diffraction Contrast Tomography and the Use of Friedel Pairs in Diffraction Data Analysis. *Rev. Sci. Instrum.* **2009**, *80*, 033905. [[CrossRef](#)]
90. Holzner, C.; Lavery, L.; Bale, H.; Merkle, A.; McDonald, S.; Withers, P.; Zhang, Y.; Jensen, D.J.; Kimura, M.; Lyckegaard, A.; et al. Diffraction Contrast Tomography in the Laboratory—Applications and Future Directions. *Microsc. Today* **2016**, *24*, 34–43. [[CrossRef](#)]
91. Johnson, G.; King, A.; Honnicke, M.G.; Marrow, J.; Ludwig, W. X-Ray Diffraction Contrast Tomography: A Novel Technique for Three-Dimensional Grain Mapping of Polycrystals. II. The Combined Case. *J. Appl. Crystallogr.* **2008**, *41*, 310–318. [[CrossRef](#)]
92. Ludwig, W.; Schmidt, S.; Lauridsen, E.M.; Poulsen, H.F. X-Ray Diffraction Contrast Tomography: A Novel Technique for Three-Dimensional Grain Mapping of Polycrystals. I. Direct Beam Case. *J. Appl. Crystallogr.* **2008**, *41*, 302–309. [[CrossRef](#)]
93. Guo, Y.; Burnett, T.L.; McDonald, S.A.; Daly, M.; Sherry, A.H.; Withers, P.J. 4D Imaging of Void Nucleation, Growth, and Coalescence from Large and Small Inclusions in Steel under Tensile Deformation. *J. Mater. Sci. Technol.* **2022**, *123*, 168–176. [[CrossRef](#)]
94. García-Moreno, F.; Kamm, P.H.; Neu, T.R.; Bülk, F.; Mokso, R.; Schlepütz, C.M.; Stampanoni, M.; Banhart, J. Using X-Ray Tomoscopy to Explore the Dynamics of Foaming Metal. *Nat. Commun.* **2019**, *10*, 3762. [[CrossRef](#)]
95. Wilkinson, A.J.; Meaden, G.; Dingley, D.J. High-Resolution Elastic Strain Measurement from Electron Backscatter Diffraction Patterns: New Levels of Sensitivity. *Ultramicroscopy* **2006**, *106*, 307–313. [[CrossRef](#)] [[PubMed](#)]
96. Di Gioacchino, F.; Quinta da Fonseca, J. Plastic Strain Mapping with Sub-Micron Resolution Using Digital Image Correlation. *Exp. Mech.* **2013**, *53*, 743–754. [[CrossRef](#)]
97. Zaeferrer, S.; Elhami, N.N. Theory and Application of Electron Channelling Contrast Imaging under Controlled Diffraction Conditions. *Acta Mater.* **2014**, *75*, 20–50. [[CrossRef](#)]
98. Nemcko, M.J.; Li, J.; Wilkinson, D.S. Effects of Void Band Orientation and Crystallographic Anisotropy on Void Growth and Coalescence. *J. Mech. Phys. Solids* **2016**, *95*, 270–283. [[CrossRef](#)]

99. Vasilev, E.; Knezevic, M. Experimental Characterization of Voids and Surrounding Microstructures Developed under Tension of Mg, Mg–3Zn, and Ti: A Statistical Study. *Mater. Sci. Eng. A* **2023**, *862*, 144411. [[CrossRef](#)]
100. Barrioz, P.O.; Hure, J.; Tanguy, B. Effect of Dislocation Channeling on Void Growth to Coalescence in FCC Crystals. *Mater. Sci. Eng. A* **2019**, *749*, 255–270. [[CrossRef](#)]
101. Wciślik, W.; Pała, R. Some Microstructural Aspects of Ductile Fracture of Metals. *Materials* **2021**, *14*, 4321. [[CrossRef](#)]
102. Pathak, N.; Adrien, J.; Butcher, C.; Maire, E.; Worswick, M. Experimental Stress State-Dependent Void Nucleation Behavior for Advanced High Strength Steels. *Int. J. Mech. Sci.* **2020**, *179*, 105661. [[CrossRef](#)]
103. Bonora, N.; Testa, G.; Ruggiero, A.; Iannitti, G.; Gentile, D. Continuum Damage Mechanics Modelling Incorporating Stress Triaxiality Effect on Ductile Damage Initiation. *Fatigue Fract. Eng. Mater. Struct.* **2020**, *43*, 1755–1768. [[CrossRef](#)]
104. Patra, A.; McDowell, D.L. A Void Nucleation and Growth Based Damage Framework to Model Failure Initiation Ahead of a Sharp Notch in Irradiated Bcc Materials. *J. Mech. Phys. Solids* **2015**, *74*, 111–135. [[CrossRef](#)]
105. McClintock, F.A. A Criterion for Ductile Fracture by the Growth of Holes. *J. Appl. Mech.* **1968**, *35*, 363–371. [[CrossRef](#)]
106. Rice, J.R.; Tracey, D.M. On the Ductile Enlargement of Voids in Triaxial Stress Fields. *J. Mech. Phys. Solids* **1969**, *17*, 201–217. [[CrossRef](#)]
107. Tvergaard, V. Material Failure by Void Growth to Coalescence. *Adv. Appl. Mech.* **1989**, *27*, 83–151. [[CrossRef](#)]
108. Tvergaard, V. On Localization in Ductile Materials Containing Spherical Voids. *Int. J. Fract.* **1982**, *18*, 237–252. [[CrossRef](#)]
109. Chu, C.C.; Needleman, A. Void Nucleation Effects in Biaxially Stretched Sheets. *J. Eng. Mater. Technol.* **1980**, *102*, 249–256. [[CrossRef](#)]
110. Hu, Y.; Feng, G.; Li, S.; Sheng, W.; Zhang, C. Numerical Modelling of Ductile Fracture in Steel Plates with Non-Ordinary State-Based Peridynamics. *Eng. Fract. Mech.* **2020**, *225*, 106446. [[CrossRef](#)]
111. Lee, H.W.; Basaran, C. A Review of Damage, Void Evolution, and Fatigue Life Prediction Models. *Metals* **2021**, *11*, 609. [[CrossRef](#)]
112. Benzerga, A.A.; Leblond, J.-B. Ductile Fracture by Void Growth to Coalescence. *Adv. Appl. Mech.* **2010**, *44*, 169–305. [[CrossRef](#)]
113. Aldakheel, F.; Wriggers, P.; Miehe, C. A Modified Gurson-Type Plasticity Model at Finite Strains: Formulation, Numerical Analysis and Phase-Field Coupling. *Comput. Mech.* **2018**, *62*, 815–833. [[CrossRef](#)]
114. Johnson, G.R.; Cook, W.H. Fracture Characteristics of Three Metals Subjected to Various Strains, Strain Rates, Temperatures and Pressures. *Eng. Fract. Mech.* **1985**, *21*, 31–48. [[CrossRef](#)]
115. Pang, W.W.; Zhang, P.; Zhang, G.C.; Xu, A.G.; Zhao, X.G. Dislocation Creation and Void Nucleation in FCC Ductile Metals under Tensile Loading: A General Microscopic Picture. *Sci. Rep.* **2014**, *4*, 6981. [[CrossRef](#)] [[PubMed](#)]
116. Agarwal, G.; Dongare, A.M. Defect and Damage Evolution during Spallation of Single Crystal Al: Comparison between Molecular Dynamics and Quasi-Coarse-Grained Dynamics Simulations. *Comput. Mater. Sci.* **2018**, *145*, 68–79. [[CrossRef](#)]
117. Cui, Y.; Chen, Z. Void Initiation from Interfacial Debonding of Spherical Silicon Particles inside a Silicon-Copper Nanocomposite: A Molecular Dynamics Study. *Model. Simul. Mat. Sci. Eng.* **2017**, *25*, 025007. [[CrossRef](#)]
118. Pogorelko, V.V.; Mayer, A.E. Influence of Copper Inclusions on the Strength of Aluminum Matrix at High-Rate Tension. *Mater. Sci. Eng. A* **2015**, *642*, 351–359. [[CrossRef](#)]
119. Pogorelko, V.V.; Mayer, A.E. Influence of Titanium and Magnesium Nano-inclusions on the Strength of Aluminum at High-Rate Tension: Molecular Dynamics Simulations. *Mater. Sci. Eng. A* **2016**, *662*, 227–240. [[CrossRef](#)]
120. Zhao, Q.Q.; Boyce, B.L.; Sills, R.B. Micromechanics of Void Nucleation and Early Growth at Incoherent Precipitates: Lattice-Trapped and Dislocation-Mediated Delamination Modes. *Crystals* **2021**, *11*, 45. [[CrossRef](#)]
121. Paul, S.K.; Kumar, S.; Tarafder, S. Effect of Loading Conditions on Nucleation of Nano Void and Failure of Nanocrystalline Aluminum: An Atomistic Investigation. *Eng. Fract. Mech.* **2017**, *176*, 257–262. [[CrossRef](#)]
122. Traiviratana, S.; Bringa, E.M.; Benson, D.J.; Meyers, M.A. Void Growth in Metals: Atomistic Calculations. *Acta Mater.* **2008**, *56*, 3874–3886. [[CrossRef](#)]
123. Tang, T.; Kim, S.; Horstemeyer, M.F. Molecular Dynamics Simulations of Void Growth and Coalescence in Single Crystal Magnesium. *Acta Mater.* **2010**, *58*, 4742–4759. [[CrossRef](#)]
124. Mi, C.; Buttry, D.A.; Sharma, P.; Kouris, D.A. Atomistic Insights into Dislocation-Based Mechanisms of Void Growth and Coalescence. *J. Mech. Phys. Solids* **2011**, *59*, 1858–1871. [[CrossRef](#)]
125. Deng, Q.-Q.; Gao, Y.-J.; Liu, Z.-Y.; Huang, Z.-J.; Li, Y.-X.; Luo, Z.-R. Atomistic Simulation of Void Growth by Emitting Dislocation Pair during Deformation. *Phys. B Condens. Matter.* **2020**, *578*, 411767. [[CrossRef](#)]
126. Xu, S.Z.; Hao, Z.M.; Su, Y.Q.; Yu, Y.; Wan, Q.; Hu, W.J. An Analysis on Nanovoid Growth in Body-Centered Cubic Single Crystalline Vanadium. *Comput. Mater. Sci.* **2011**, *50*, 2411–2421. [[CrossRef](#)]
127. Zhao, L.; Liu, Y. Investigation on Void Growth and Coalescence in Single Crystal Copper under High-Strain-Rate Tensile Loading by Atomistic Simulation. *Mech. Mater.* **2020**, *151*, 103615. [[CrossRef](#)]
128. Wang, J.P.; Liang, J.W.; Wen, Z.X.; Yue, Z.F. Atomic Simulation of Void Location Effect on the Void Growth in Nickel-Based Single Crystal. *Comput. Mater. Sci.* **2019**, *160*, 245–255. [[CrossRef](#)]
129. Tang, Y.; Bringa, E.M.; Remington, B.A.; Meyers, M.A. Growth and Collapse of Nanovoids in Tantalum Monocrystals. *Acta Mater.* **2011**, *59*, 1354–1372. [[CrossRef](#)]
130. Zhang, Y.; Jiang, S.; Zhu, X.; Zhao, Y. Dislocation Mechanism of Void Growth at Twin Boundary of Nanotwinned Nickel Based on Molecular Dynamics Simulation. *Phys. Lett. A* **2016**, *380*, 2757–2761. [[CrossRef](#)]

131. Qi, Y.; Chen, X.; Feng, M. Effect of Void Defect on C-Axis Deformation of Single-Crystal Ti under Uniaxial Stress Conditions: Evolution of Tension Twinning and Dislocations. *J. Mater. Res.* **2019**, *34*, 3699–3706. [\[CrossRef\]](#)
132. Xu, X.-T.; Tang, F.-L.; Xue, H.-T.; Yu, W.-Y.; Zhu, L.; Rui, Z.-Y. Molecular Dynamics Simulations of Void Shrinkage in γ -TiAl Single Crystal. *Comput. Mater. Sci.* **2015**, *107*, 58–65. [\[CrossRef\]](#)
133. Zhang, Y.; Jiang, S.; Zhu, X.; Zhao, Y. Influence of Void Density on Dislocation Mechanisms of Void Shrinkage in Nickel Single Crystal Based on Molecular Dynamics Simulation. *Phys. E Low Dimens. Syst. Nanostruct.* **2017**, *90*, 90–97. [\[CrossRef\]](#)
134. Yang, X.; Zeng, X.; Wang, J.; Wang, J.; Wang, F.; Ding, J. Atomic-Scale Modeling of the Void Nucleation, Growth, and Coalescence in Al at High Strain Rates. *Mech. Mater.* **2019**, *135*, 98–113. [\[CrossRef\]](#)
135. Rawat, S.; Raole, P.M. Molecular Dynamics Investigation of Void Evolution Dynamics in Single Crystal Iron at Extreme Strain Rates. *Comput. Mater. Sci.* **2018**, *154*, 393–404. [\[CrossRef\]](#)
136. Potirniche, G.P.; Horstemeyer, M.F.; Wagner, G.J.; Gullett, P.M. A Molecular Dynamics Study of Void Growth and Coalescence in Single Crystal Nickel. *Int. J. Plast.* **2006**, *22*, 257–278. [\[CrossRef\]](#)
137. Liu, B.; Qiu, X.; Huang, Y.; Hwang, K.C.; Li, M.; Liu, C. The Size Effect on Void Growth in Ductile Materials. *J. Mech. Phys. Solids* **2003**, *51*, 1171–1187. [\[CrossRef\]](#)
138. Li, Z.; Steinmann, P. RVE-Based Studies on the Coupled Effects of Void Size and Void Shape on Yield Behavior and Void Growth at Micron Scales. *Int. J. Plast.* **2006**, *22*, 1195–1216. [\[CrossRef\]](#)
139. Segurado, J.; Llorca, J. An Analysis of the Size Effect on Void Growth in Single Crystals Using Discrete Dislocation Dynamics. *Acta Mater.* **2009**, *57*, 1427–1436. [\[CrossRef\]](#)
140. Cheng, Z.; Zhang, C.; Meng, Z.; Wang, K.; Chen, L.; Ji, Z.; Zhao, G. Coupled Crystal Plasticity and Micromechanics Damage Model Based on Viscoplastic Self-Consistent Theory and x-Ray Computed Tomography. *Int. J. Plast.* **2023**, *160*, 103511. [\[CrossRef\]](#)
141. Ha, S.; Kim, K. Void Growth and Coalescence in f.c.c. Single Crystals. *Int. J. Mech. Sci.* **2010**, *52*, 863–873. [\[CrossRef\]](#)
142. Liu, J.; Huang, M.; Li, Z.; Zhao, L.; Zhu, Y. Microvoid Growth Mechanism in FCC Polycrystals and a Statistical Damage Model. *Int. J. Plast.* **2021**, *137*, 102888. [\[CrossRef\]](#)
143. Zhu, J.; Liu, J.; Huang, M.; Li, Z.; Zhao, L. Investigation on Intragranular and Intergranular Void Growth and Their Competition in Polycrystalline Materials. *Int. J. Plast.* **2022**, *159*, 103472. [\[CrossRef\]](#)
144. Liu, W.H.; He, Z.T.; Tang, J.G.; Hu, Z.J.; Cui, D.T. The Effects of Load Condition on Void Coalescence in FCC Single Crystals. *Comput. Mater. Sci.* **2012**, *60*, 66–74. [\[CrossRef\]](#)
145. Christodoulou, P.G.; Dancette, S.; Lebensohn, R.A.; Maire, E.; Beyerlein, I.J. Role of Crystallographic Orientation on Intragranular Void Growth in Polycrystalline FCC Materials. *Int. J. Plast.* **2021**, *147*, 103104. [\[CrossRef\]](#)
146. Jeong, W.; Lee, C.H.; Moon, J.; Jang, D.; Lee, M.G. Grain Scale Representative Volume Element Simulation to Investigate the Effect of Crystal Orientation on Void Growth in Single and Multi-Crystals. *Metals* **2018**, *8*, 436. [\[CrossRef\]](#)
147. Guo, H.J.; Li, D.F. Crystal Plasticity-Based Micromechanical Finite Element Modelling of Ductile Void Growth for an Aluminium Alloy under Multiaxial Loading Conditions. *Proc. Inst. Mech. Eng. Part L J. Mater. Des. Appl.* **2019**, *233*, 52–62. [\[CrossRef\]](#)
148. Dakshinamurthy, M.; Kowalczyk-Gajewska, K.; Vadillo, G. Influence of Crystallographic Orientation on the Void Growth at the Grain Boundaries in Bi-Crystals. *Int. J. Solids Struct.* **2021**, *212*, 61–79. [\[CrossRef\]](#)
149. Asim, U.; Siddiq, M.A.; Demiral, M. Void Growth in High Strength Aluminium Alloy Single Crystals: A CPFEM Based Study. *Model. Simul. Mat. Sci. Eng.* **2017**, *25*, 035010. [\[CrossRef\]](#)
150. Guo, H.J.; Ling, C.; Busso, E.P.; Zhong, Z.; Li, D.F. Crystal Plasticity Based Investigation of Micro-Void Evolution under Multi-Axial Loading Conditions. *Int. J. Plast.* **2020**, *129*, 102673. [\[CrossRef\]](#)
151. Liu, W.; Zhang, X.; Tang, J. Study on the Growth Behavior of Voids Located at the Grain Boundary. *Mech. Mater.* **2009**, *41*, 799–809. [\[CrossRef\]](#)
152. Pushkareva, M.; Sket, F.; Segurado, J.; Llorca, J.; Yandouzi, M.; Weck, A. Effect of Grain Orientation and Local Strains on Void Growth and Coalescence in Titanium. *Mater. Sci. Eng. A* **2019**, *760*, 258–266. [\[CrossRef\]](#)
153. Zhu, J.C.; Bettaieb, M.B.; Abed-Meraim, F.; Huang, M.S.; Li, Z.H. Coupled Effects of Crystallographic Orientation and Void Shape on Ductile Failure Initiation Using a CPFE Framework. *Eng. Fract. Mech.* **2023**, *280*, 109121. [\[CrossRef\]](#)
154. Asim, U.B.; Siddiq, M.A.; Kartal, M.E. A CPFEM Based Study to Understand the Void Growth in High Strength Dual-Phase Titanium Alloy (Ti-10V-2Fe-3Al). *Int. J. Plast.* **2019**, *122*, 188–211. [\[CrossRef\]](#)
155. Selvarajou, B.; Joshi, S.P.; Benzerger, A.A. Void Growth and Coalescence in Hexagonal Close Packed Crystals. *J. Mech. Phys. Solids* **2019**, *125*, 198–224. [\[CrossRef\]](#)
156. Jung, J.; Lefeld-sosnowska, M. High-Pressure-Induced Defect Formation in Silicon Single Crystals I. Characterization of Defects and Conditions of Their Creation. *Philos. Mag. A Phys. Condens. Matter Struct. Defects Mech. Prop.* **1985**, *50*, 233–255. [\[CrossRef\]](#)
157. Lewandowski, J.J.; Lowhaphandu, P. Effects of Hydrostatic Pressure on Mechanical Behaviour and Deformation Processing of Materials. *Int. Mater. Rev.* **1998**, *43*, 145–187. [\[CrossRef\]](#)
158. Bridgman, P.W. The Effect of Hydrostatic Pressure on the Fracture of Brittle Substances. *J. Appl. Phys.* **1947**, *18*, 246–258. [\[CrossRef\]](#)
159. Bridgman, P.W. The Effect of Pressure on the Tensile Properties of Several Metals and Other Materials. *J. Appl. Phys.* **1953**, *24*, 560–570. [\[CrossRef\]](#)
160. Spitzig, W.A.; Richmond, O. The Effect of Pressure on the Flow Stress of Metals. *Acta Metall.* **1984**, *32*, 457–463. [\[CrossRef\]](#)
161. Spitzig, W.A.; Sober, R.J.; Richmond, O. The Effect of Hydrostatic Pressure on the Deformation Behavior of Maraging and HY-80 Steels and Its Implications for Plasticity Theory. *Metall. Trans. A* **1976**, *7*, 1703–1710. [\[CrossRef\]](#)

162. Jung, J. A Note on the Influence of Hydrostatic Pressure on Dislocations. *Philos. Mag. A Phys. Condens. Matter Struct. Defects Mech. Prop.* **1981**, *43*, 1057–1061. [[CrossRef](#)]
163. Pines, B.Y.; Syrenko, A.F. Change of Dislocation Density in Aluminium and Lithium Fluoride after Annealing near the Melting Point under Hydrostatic Pressure. *J. Mater. Sci.* **1968**, *3*, 80–88. [[CrossRef](#)]
164. Bulatov, V.V.; Richmond, O.; Glazov, M. V An Atomistic Dislocation Mechanism of Pressure-Dependent Plastic Flow in Aluminum. *Acta Mater.* **1999**, *47*, 3507–3514. [[CrossRef](#)]
165. Ohashi, T. Generation and Accumulation of Atomic Vacancies Due to Dislocation Movement and Pair Annihilation. *Philos. Mag.* **2018**, *98*, 2275–2295. [[CrossRef](#)]
166. Couch, W.E.; Swartz, J.C. The Dilatation of Dislocation Kinks and Jogs. *Philos. Mag.* **1962**, *7*, 1231–1238. [[CrossRef](#)]
167. Frafjord, J.; Ringdalen, I.G.; Hopperstad, O.S.; Holmestad, R.; Friis, J. First Principle Calculations of Pressure Dependent Yielding in Solute Strengthened Aluminium Alloys. *Comput. Mater. Sci.* **2020**, *184*, 109902. [[CrossRef](#)]
168. Ashby, M.F.; Verrall, R.A. Micromechanisms of Flow and Fracture, and Their Relevance to the Theology of the Upper Mantle. *Phil. Trans. R. Soc. Lond. A* **1977**, *288*, 59–95.
169. Shmatov, V.T. Lattice Resistance to Dislocation Motion under Hydrostatic Pressure. *Phys. Met. Metallogr.* **1973**, *35*, 47–55.
170. Brown, J.L.; Prime, M.B.; Barton, N.R.; Luscher, D.J.; Burakovsky, L.; Orlikowski, D. Experimental Evaluation of Shear Modulus Scaling of Dynamic Strength at Extreme Pressures. *J. Appl. Phys.* **2020**, *128*, 045901. [[CrossRef](#)]
171. Prime, M.B.; Arsenlis, A.; Austin, R.A.; Barton, N.R.; Battaile, C.C.; Brown, J.L.; Burakovsky, L.; Buttler, W.T.; Chen, S.R.; Dattelbaum, D.M.; et al. A Broad Study of Tantalum Strength from Ambient to Extreme Conditions. *Acta Mater.* **2022**, *231*, 117875. [[CrossRef](#)]
172. Auger, J.P.; Francois, D. Variation of Fracture Toughness of a 7075 Aluminium Alloy with Hydrostatic Pressure and Relationship with Tensile Ductility. *Int. J. Fract.* **1977**, *13*, 431–441. [[CrossRef](#)]
173. Spitzig, W.A.; Sober, R.J.; Richmond, O. Pressure Dependence of Yielding and Associated Volume Expansion in Tempered Martensite. *Acta Metall.* **1975**, *23*, 885–893. [[CrossRef](#)]
174. Yajima, M.; Ishii, M. The Effect of Hydrostatic Pressure on Yielding in Iron. *Trans. ISIJ* **1967**, *7*, 45–52. [[CrossRef](#)]
175. Margevicius, R.W.; Lewandowski, J.J.; Locci, I. The Decrease in Yield Strength in NiAl Due to Hydrostatic Pressure. *Scr. Metall. Mater.* **1992**, *26*, 1733–1736. [[CrossRef](#)]
176. Margevicius, R.W.; Lewandowski, J.J. The Effects of Hydrostatic Pressure on the Mechanical Behaviour of NiAl. *Scr. Metall.* **1991**, *25*, 2017–2022. [[CrossRef](#)]
177. Weaver, M.L.; Noebe, R.; Lewandowski, J.J.; Oliver, B.F.; Kaufman, M. The Effects of Interstitial Content, Heat Treatment, and Prestrain on the Tensile Properties of NiAl. *Mater. Sci. Eng. A* **1995**, *192–193*, 179–185. [[CrossRef](#)]
178. Ashby, M.F.; Gelles, S.H.; Tanner, L.E. The Stress at Which Dislocations Are Generated at a Particle-Matrix Interface. *Philos. Mag.* **1969**, *19*, 757–771. [[CrossRef](#)]
179. Mott, N.F.; Nabarro, F.R.N. An Attempt to Estimate the Degree of Precipitation Hardening, with a Simple Model. *Proc. Phys. Soc.* **1940**, *52*, 86–89. [[CrossRef](#)]
180. Liu, D.-S. *The Effects of Superimposed Pressure on the Deformation and Fracture of Metal-Matrix Composites*; Case Western Reserve University: Cleveland, OH, USA, 1991.
181. Vasudevan, A.K.; Richmond, O. The Influence of Hydrostatic Pressure on the Ductility of Al-SiC Composites. *Mater. Sci. Eng.* **1989**, *A107*, 63–69. [[CrossRef](#)]
182. Sakamoto, H.; Iizuka, T. FEM Analysis on Fundamental Relationship between Hydrostatic Stress and Strain Obtained from Uniaxial Tensile Test Using Axially Symmetric Tapered Specimen. In Proceedings of the XIV International Conference on Computational Plasticity: Fundamentals and Applications, Barcelona, Spain, 5–7 September 2017; Onate, E., Owen, D.R.J., Peric, D., Chiumenti, M., Eds.; CIMNE: Barcelona, Spain, 2017; pp. 5–7.
183. Thomason, P.F. *Ductile Fracture of Metals*; Pergamon Press: New York, NY, USA, 1990.
184. Brown, L.M.; Stobbs, W.M. The Work-Hardening of Copper-Silica v. Equilibrium Plastic Relaxation by Secondary Dislocations. *Philos. Mag.* **1976**, *34*, 351–372. [[CrossRef](#)]
185. Argon, A.S.; Im, J.; Safoglu, R. Cavity Formation from Inclusions Inductile Fracture. *Metall. Trans. A* **1975**, *6*, 825–837. [[CrossRef](#)]
186. French, I.E.; Weinrich, P.F. The Effect of Hydrostatic Pressure on the Tensile Fracture of α -Brass. *Acta Metall.* **1973**, *21*, 1533–1537. [[CrossRef](#)]
187. Gonzalez, C.; Llorca, J. An Analysis of the Effect of Hydrostatic Pressure on the Tensile Deformation of Aluminium-Matrix Composites. *Mater. Sci. Eng. A* **2003**, *341*, 256–263. [[CrossRef](#)]
188. Liu, D.S.; Lewandowski, J.J. The Effects of Superimposed Hydrostatic Pressure on Deformation and Fracture: Part II. Particulate-Reinforced 6061 Composites. *Metall. Trans. A* **1993**, *24*, 609–615. [[CrossRef](#)]
189. Liu, D.S.; Manoharan, M.; Lewandowski, J.J. Matrix Effects on the Ductility of Aluminium-Based Composites Deformed under Hydrostatic Pressure. *J. Mater. Sci. Lett.* **1989**, *8*, 1447–1448. [[CrossRef](#)]
190. Lahaie, D.J.; Embury, J. Hydrostatic Extrusion of Metal Matrix Composites. *J. Compos. Mater.* **2003**, *37*, 1589–1599. [[CrossRef](#)]

191. Lee, M.-G.; Korkolis, Y.P.; Kim, J.H. Recent Developments in Hydroforming Technology. *Proc. Inst. Mech. Eng. B J. Eng. Manuf.* **2015**, *229*, 572–596. [[CrossRef](#)]
192. Zok, F.; Embury, J. Forming of Low-Ductility Materials under Hydrostatic Pressure. *J. Mater. Shap. Technol.* **1990**, *8*, 77–81. [[CrossRef](#)]
193. Ashby, M.F. The Deformation of Plastically Non-Homogeneous Materials. *Philos. Mag.* **1970**, *21*, 399–424. [[CrossRef](#)]

Disclaimer/Publisher’s Note: The statements, opinions and data contained in all publications are solely those of the individual author(s) and contributor(s) and not of MDPI and/or the editor(s). MDPI and/or the editor(s) disclaim responsibility for any injury to people or property resulting from any ideas, methods, instructions or products referred to in the content.